nature reviews earth & environment

https://doi.org/10.1038/s43017-024-00573-7

Review article

Check for updates

The Indian Ocean Dipole in a warming world

Guojian Wang[1] ✉, Wenju Cai[2,3,4,5] ✉, Agus Santoso[1,6,7], Nerilie Abram[8,9,10], Benjamin Ng[1], Kai Yang[1,11], Tao Geng[2,3], Takeshi Doi[12], Yan Du[13,14], Takeshi Izumo[15], Karumuri Ashok[16,17], Jianping Li[3,18], Tim Li[19,20], Sebastian McKenna[6], Shuangwen Sun[21,22,23], Tomoki Tozuka[24], Xiaotong Zheng[2,3], Yi Liu[1,2], Lixin Wu[2,3], Fan Jia[3,25], Shijian Hu[3,25] & Xichen Li[26]

Abstract

The Indian Ocean Dipole (IOD) strongly affects the climate of the Indo-Pacific. Observations suggest a shift towards stronger and earlier positive IOD (pIOD) events alongside an increased amplitude of sea surface temperature (SST) anomalies, but uncertainty remains, impeding assessments of ongoing changes. In this Review, we synthesize the available knowledge of projected changes in the IOD during the twenty-first century under anthropogenic warming. Compared to observations, models struggle to simulate the Bjerknes feedback, asymmetry in the strength of positive and negative IOD anomalies and El Niño–Southern Oscillation or monsoonal forcings. Yet several models do capture important feedbacks reasonably well and offer useful tools with which to assess IOD evolution. A pIOD-like SST warming pattern (an enhanced west-minus-east SST gradient) alongside shifts in feedback process drive corresponding changes to the IOD. Over the course of the twenty-first century, robust changes include: enhanced IOD SST variability (as measured by the first principal component of spring SST variability, not the dipole mode index); an increase in strong rainfall pIOD events; an increase and decrease in the frequency of strong-pIOD and moderate-pIOD, respectively, as defined by SST; and an increase in the frequency of early-pIOD events. Palaeo evidence reveals similar increases in the magnitude and frequency of pIOD events underpinned by a similar pattern of mean state change (Last Glacial Maximum, post-1960), reinforcing IOD projections. Sustained international efforts are needed to improve IOD simulations and reduce projection uncertainties.

Sections

A full list of affiliations appears at the end of the paper. ✉e-mail: Guojian.Wang@csiro.au; Wenju.Cai@csiro.au

Introduction

The IOD is the dominant mode of interannual climate variability in the tropical Indian Ocean. It is characterized by an SST seesaw between the western and eastern tropical Indian Ocean[1–3], wherein a pIOD exhibits negative SST anomalies off Sumatra and Java, and positive SST anomalies off east Africa; the converse is true for a negative IOD (nIOD). The IOD exhibits distinct seasonality, developing during austral winter (June, July and August; JJA) and maturing into spring (September, October and November; SON).

These changes in SST and heat transport have marked climatic, ecological and societal impacts. For instance, pIOD events dampen biological activity (chlorophyll *a*) in the western Indian Ocean owing to warm water convergence and depressed upwelling, whereas intensified upwelling enhances biological activity in the eastern Indian Ocean[4,5]. Climatically, pIOD-related SST anomalies strengthen the zonal west-minus-east SST gradient, shifting deep atmospheric convection westward[6], promoting increased rainfall and flooding (and corresponding landslides and malaria outbreaks[7–9]) in east Africa[10–14], but drought in Indonesia and southeastern Australia. Indeed, the strong 2019 pIOD event displaced millions of people across Africa away from flooding[9] and contributed to the devastating 'black summer' bushfires across southeastern and eastern Australia, which caused the deaths of more than one billion animals, the destruction of 59,000 buildings[15,16], and the release of 700 million tonnes of carbon dioxide[17]. Further afield, pIOD-induced atmospheric circulation anomalies contribute to reduced rainfall over Europe, northeast Asia and South America[18,19], and suppressed tropical cyclone activity in the Atlantic[20,21].

These effects highlight a clear societal need to understand how the IOD might respond to greenhouse warming. However, deciphering these changes is a complex issue. On the one hand, climate models reveal no inter-model agreement in projected changes when using a conventional IOD index — the dipole mode index (DMI) — based on fixed regions of the western and eastern Indian Ocean[22,23]. On the other hand, models consistently project faster warming in the western equatorial Indian Ocean (EIO) than in the eastern EIO[22–28], establishing a pIOD-like warming pattern that features an increase in the west-minus-east mean SST gradient and a corresponding increase in pIOD events with strong rainfall anomalies[6].

In this Review, we synthesize knowledge on how the IOD might respond to a warming climate in the twenty-first century. We begin with a description of observed fundamental IOD characteristics, including its forcings, feedbacks, diversity and teleconnection. We follow with a discussion of how these processes are simulated in the latest climate models participating in the Coupled Model Intercomparison Project phase 6 (CMIP6) (ref. 29). Projected changes in the mean state, IOD feedbacks and IOD SST variability are subsequently assessed, followed by discussion of influences from the mean state change and possible modulating factors, including ENSO–IOD and monsoon–IOD interactions, mean state bias and internal variability. We then synthesize insights into IOD properties and changes from palaeo-proxy data. The Review ends with a discussion of research priorities.

Indian Ocean Dipole dynamics and characteristics

Examination of the IOD and its changes relies on observations. In the Indian Ocean, however, such observations were sparse before the mid-twentieth century (particularly for SST[30–32]), and exhibit substantial differences across products even after 1990 (refs. 33–35): for example, ERSST[36] and HadISST[37] cannot fully capture magnitude of strong pIOD events in 1997 and 2019 (Supplementary Fig. 1). Nevertheless, observational and reanalysis products are frequently used to assess historical variability of the IOD and validate climate models that are used to make future projections. Here, the major characteristics and properties of the IOD are described using the multi-product mean of more realistic SST products[38–42] (Supplementary Fig. 1), focusing on feedbacks, forcings, teleconnections, diversity and changes.

Processes of IOD lifecycle

pIOD events emerge through various dynamical and thermodynamical feedback processes, including the Bjerknes feedback, the wind–evaporation–SST feedback and the SST–cloud–radiation feedback. Bjerknes feedback effectively operates during JJA and SON when favourable climatological conditions occur — boreal summer Asian monsoon-related[23,43–45] southeasterly winds along the Sumatra–Java coast that produce a mean shallow thermocline in the east (Fig. 1a), allowing upwelling to influence the surface and strengthen air–sea coupling[43,46]. Specifically, easterly wind anomalies induce enhanced upwelling and shoal the thermocline in the eastern EIO, cooling the sea surface; the strong west-minus-east SST gradient, in turn, strengthens the easterly wind anomalies[23]; equatorial easterly anomalies drive a southern off-equatorial downwelling Rossby wave; the Rossby wave reflects as a downwelling Kelvin wave at the western boundary, driving anomalous Ekman pumping and warm SST anomalies in the western EIO[47–50]. In addition, increased wind speeds from the superposition of easterly anomalies onto climatological easterlies enhance eastern EIO SST cooling via wind–evaporation–SST feedback[23]. In turn, cooling off Sumatra–Java suppresses local atmospheric convection, increasing downward shortwave radiation that warms the surface and dampens negative SST anomalies through the SST–cloud–radiation feedback[23].

Nonlinear processes are also integral to IOD dynamics[6,49,51,52]. During SON in particular, exceptionally strong easterly wind anomalies cause nonlinear zonal advection[6,49], cooling the eastern EIO by transporting heat towards the western EIO. Concurrently, anomalous upwelling and vertical temperature gradients cause nonlinear vertical advection, bringing colder deep water to the surface[23,51,53–55]. These two nonlinear advection terms reinforce the growth of high-magnitude cool eastern EIO SST anomalies, as evident during strong pIOD events in 1961, 1994, 1997, 2006 and 2019 (refs. 6,49,51,52) (Fig. 1b). These collective air–sea feedbacks usually operate until the IOD reaches maturity into austral spring.

Following maturity, shifting climatological conditions cause the termination of pIOD events. Specifically, the onset of the austral summer Australian monsoon in early December reverses the climatological winds to westerlies. The thermocline subsequently deepens, upwelling stops, and easterly anomalies offset the climatological westerlies, which are not conducive to the growth of cold eastern EIO SST anomalies through the wind–evaporation–SST feedback[56]. These actions rapidly terminate the pIOD event.

During nIOD events, SST anomalies (warming in the eastern EIO, cooling in the western EIO) are generally more subdued than for pIOD events owing to weaker feedbacks. Bjerknes feedbacks operate in the opposite manner to pIOD: westerly wind anomalies deepen the thermocline in the eastern EIO, warming the sea surface; the decreased west-minus-east SST gradient, in turn, strengthens the westerly wind anomalies; equatorial westerly anomalies drive a southern off-equatorial upwelling Rossby wave; the Rossby wave reflects as an upwelling Kelvin wave at the western boundary, cooling SST anomalies in the western EIO. The SST responses to thermocline depth (the thermocline feedback) are much weaker compared to pIOD events, largely because the

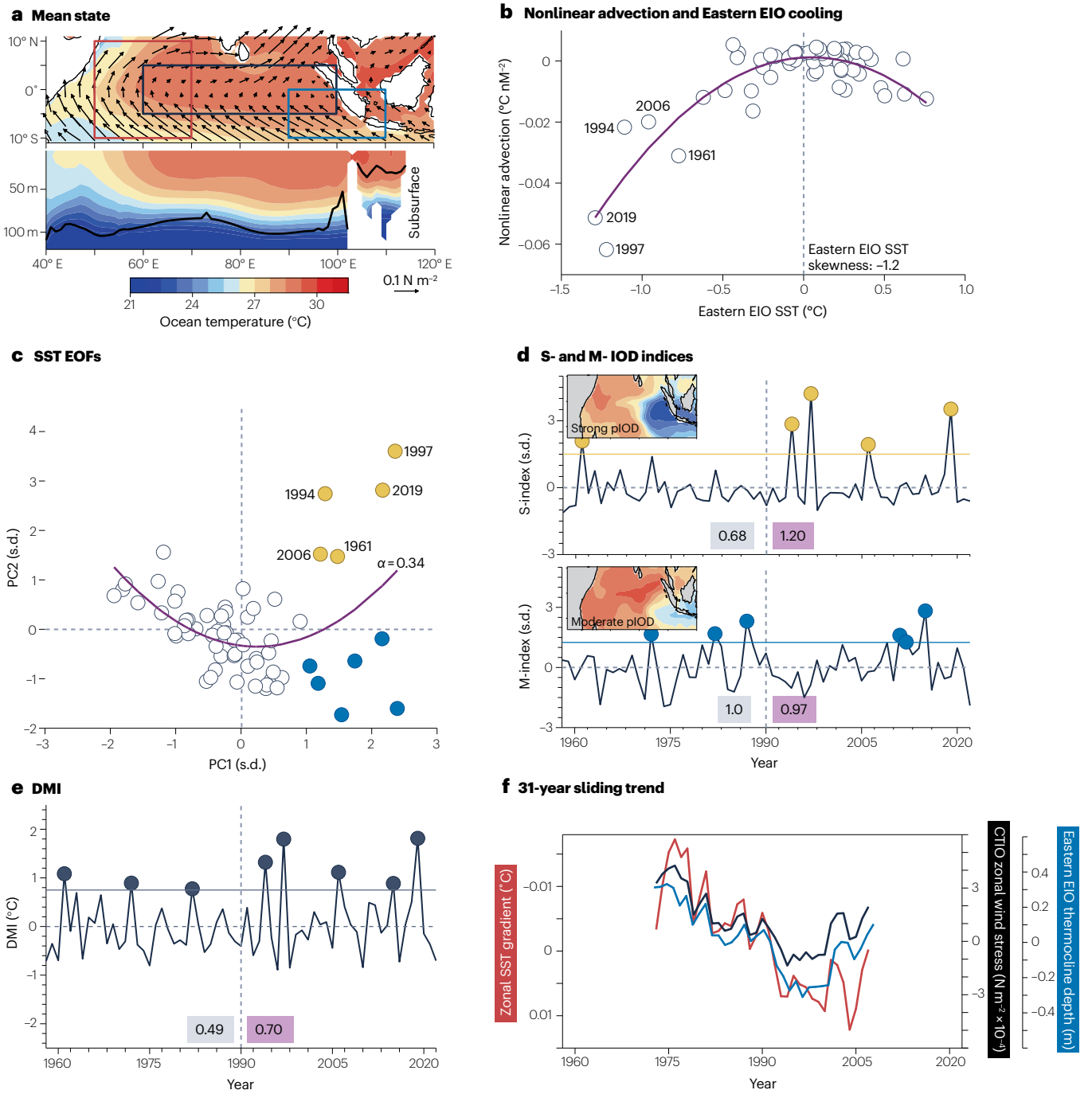

Fig. 1 | The observed characteristics and changes in the Indian Ocean Dipole since 1958. a, June–November climatological mean SST (upper panel, shading), surface wind stress (upper panel, arrows) and 5°S–5°N averaged subsurface temperature (lower panel, shading) and thermocline depth (lower panel, black contour) in 1958–2022. **b**, Relationship between nonlinear advection feedbacks and eastern equatorial Indian Ocean (EIO) SST, expressed as a quadratic nonlinear function (purple). **c**, The relationship between the normalized first two principal components (PC1 and PC2) of springtime (September–November) tropical Indian Ocean SST, expressed as a nonlinear function (purple). Yellow dots indicate positive Indian Ocean Dipole (pIOD) events in the strong regime, wherein the S-index (calculated as (PC1 + PC2)/√2)) is >1.5 standard deviations (s.d.), and blue dots indicate pIOD events in the moderate regime, where the M-index (calculated as (PC1 − PC2)/√2)) is >1.25 s.d. **d**, Timeseries and SST spatial patterns of the S-index and M-index. **e**, The detrended spring canonical dipole mode index (DMI), with black dots representing pIOD events when the DMI is >0.75 °C. **f**, 31-year sliding trends for June–November zonal SST gradient (red; the SST difference between the western EIO (red box in **a**) and the eastern EIO (blue box in **a**)), thermocline depth (blue) over the eastern EIO, and zonal wind stress (black) over the central tropical Indian Ocean (CTIO; black box in **a**). In **d** and **e**, values in grey and pink boxes indicate the standard deviations of the index in 1958–1989 and 1990–2022, respectively. In all panels, ocean variables are the multi-product mean[38–42]. The IOD is nonlinear, with the mean state becoming more pIOD-like.

thermocline is already climatologically deep in the eastern EIO, and hence any additional thermocline deepening has minimal effect on the surface warming[23,53–55,57,58]. In contrast, the SST–cloud–radiation negative feedback is greater than for pIOD events, given that an nIOD warming-induced cloud increase over the eastern EIO does not have a limit in its curtailing effect on the SST anomalies[53]. Nonlinear advection further dampens nIOD warm anomalies in the eastern EIO. For example, as warm anomalies grow, enhanced advection from the west of water with a reduced west-minus-east gradient prevents warm signals becoming too warm[6,49,52,58] (Fig. 1b). These differences in SST anomalies between pIOD and nIOD lead to a negative eastern EIO SST skewness; by contrast, the equivalent differences are far smaller for the western EIO primarily because of the climatologically deep thermocline and, therefore, low skewness. Consequently, there is a positive skewness in the DMI[23,55,57–59].

IOD triggers and modulating factors

In addition to feedback processes, the IOD is also modulated and triggered by ENSO, largely via the Walker circulation[60,61]. Specifically, eastern equatorial Pacific surface warming associated with an El Niño weakens the Walker circulation, generating easterly wind anomalies in the equatorial Indian Ocean[46,62–64] that trigger initiation of a pIOD; La Niña events conversely trigger a nIOD through strengthening of the Walker Circulation, driving westerly wind anomalies in the equatorial Indian Ocean. However, as demonstrated by the development phase of strong pIOD events in 1961 and 2019, and a nIOD in 2016, IOD events can occur independently of ENSO[1,65,66] through processes internal to the Indian Ocean[52,67,68]. However, ENSO-forced IODs tend to develop and peak later than ENSO-independent IODs, probably due to the tendency for ENSO anomalies to peak towards austral summer[67,69].

The boreal summer Asian monsoon also strongly controls the triggering of IOD events[43,62,70]. For instance, early onset of the Bay of Bengal summer monsoon promotes equatorial easterly wind anomalies[69,71], initiating early-pIOD occurrences. These early-pIOD events develop and mature prior to austral spring, and have been observed after the 1970s, as in 2007 and 2008 (refs. 71,72). In a similar vein, the South China Sea summer monsoon can also induce a pIOD event by suppressing atmospheric convection over the Maritime Continent, favouring anomalous southeasterly winds off Sumatra and Java, as in 1961 and 2006 (refs. 73,74).

The IOD is also modulated by various other climate processes. For instance, persistent SST anomalies from the subtropical Indian Ocean Dipole (a seesaw in SST anomalies between the southwest and northeast southern Indian Ocean that peaks in December–February[75,76]) influence wind anomalies in key IOD regions. During a positive subtropical Indian Ocean Dipole, cold anomalies in the northeast southern Indian Ocean induce southeasterly wind anomalies off Sumatra–Java, conducive to the development of pIOD events[75–77], as in 1997 and 2006 (ref. 77). Arctic sea ice is also thought to affect the IOD. Positive boreal winter Arctic sea ice anomalies reduce wind speed in the subtropical Atlantic, warming SSTs through reduced evaporative cooling, in turn triggering a Rossby wave train that produces anomalous low pressure over the northern Arabian Sea, inducing a pIOD[78]. Volcanism can similarly force the IOD, as shown in models by a Pinatubo-like tropical terrestrial volcanic eruption cooling Africa, promoting westerly wind anomalies over the tropical Indian Ocean that force an nIOD event[79]. Finally, the Pacific Decadal Oscillation exerts influence on the IOD on decadal timescales. The positive phase of the Pacific Decadal Oscillation weakens the Indonesian throughflow, shoaling the eastern EIO thermocline, intensifying thermocline feedback[80–82] and promoting easterly wind anomalies along the tropical Indian Ocean[83–86] that are conducive to pIOD events.

IOD teleconnection

IOD SST anomalies trigger tropical and extratropical atmospheric teleconnections[87–89]. The tropical teleconnection is an equatorially trapped, deep baroclinic response to convective heating anomalies. pIOD-related anomalously cool SSTs in the east drive anomalous subsidence and higher-than-normal surface pressure, promoting drought conditions over Sumatra–Java. Conversely, warm SST anomalies in the west encourage anomalous ascending motion and low pressure, promoting increased rainfall over eastern Africa[10–14].

These diabatic heating anomalies also excite equivalent barotropic Rossby wave trains that propagate into the extratropics[87–89]. During a pIOD in JJA, negative convective anomalies coincide with cooler SSTs in the east[13], triggering Rossby wave trains with a Pacific South America (PSA)-like pattern. This PSA-like pattern features a high-pressure centre south of Australia, reducing the midlatitude westerlies across southern Australia and, thereby, rainfall[13,90] (Supplementary Fig. 2a). In SON, strengthened SST anomalies enhance and shift the teleconnection slightly westward[13]. The resulting PSA-like wave train curves eastward and poleward toward the Antarctic before veering equatorward along eastern South America. The high-pressure centre near the Amundsen Sea Low, for example, reduces sea ice in the Bellingshausen Sea sector[91], while other pressure centres over South America encourage anomalously high rainfall over Chile and southeastern South America[92] (Supplementary Fig. 2b). In this way, when a pIOD is concurrent with an El Niño, it reinforces El Nino's impacts[92]. During nIOD events, the teleconnections are generally opposite but a strong asymmetry exists in line with the IOD amplitude asymmetry[93].

IOD diversity

Individual IOD events can exhibit substantial diversity[49,72,76,94,95]. This diversity can be described in terms of contrasting impacts (for instance, the intensity of floods in eastern Africa and drought over Sumatra–Java[6]), contrasting forcings (for instance, whether SST anomalies are concurrent with or independent from ENSO[69,96], or whether the IOD is forced by the Asian monsoon or not[97]), contrasting development and maturity timing (for instance, whether SST anomalies develop and mature in austral winter, that is, one season earlier than the canonical IOD[71,72]), and contrasting SST patterns and intensity (for instance, the centre of maximum SST anomalies in the east or the west[49,94,95]). These contrasts are not necessarily independent and can be linked to the same external forcings. For example, the onset of the Asian monsoon can lead to either a canonical pIOD that develops in JJA and peaks in SON or an early-pIOD that matures about one season early[69,71,72].

The IOD diversity that stems from the pattern and strength of SST anomalies describes two preferred IOD regimes: strong-pIOD features the dominance of cool anomalies in the eastern pole, underpinned by nonlinear advection linked to an exceptionally strong upwelling and westward upper ocean current, while moderate-pIOD features the dominance of warm anomalies in the western pole governed by Ekman pumping[6,49]. These two pIOD regimes can be represented by an empirical orthogonal function (EOF) decomposition of SON SST anomalies over the equatorial Indian Ocean domain (Fig. 1c) (refs. 6,34,49,52), with the index for strong-pIOD events (the S-index) calculated as (PC1 + PC2)/√2), and the index for moderate-pIOD events (the M-index) calculated as (PC1 − PC2)/√2) (Fig. 1d) (ref. 49); the anomaly pattern associated with the first principal component (PC1) represents the

classic pIOD pattern, while that of the second principal component (PC2) features a westward extension of cold anomalies from off Sumatra–Java, modifying the first EOF pattern to yield inter-event diversity[34,49].

Observed changes in the IOD

Notable changes have been observed to the IOD. One such change includes an increase in the variability amplitude of the DMI underpinned by changes in the climatological tropical Indian Ocean featuring a faster warming in the west, stronger equatorial easterlies and a shallowing thermocline in the eastern EIO since the late 1950s (Fig. 1e,f). In particular, more frequent strong-pIOD events have occurred, going from one event in the pre-1990 period (1961) to four events in the post-1990 period (1994, 1997, 2006 and 2019) (refs. 6,34,44,49,52,98) (Fig. 1d). In addition, pIOD events are also developing and maturing earlier after the 1970s[71,72], consistent with an earlier onset of the Bay of Bengal monsoon or the South China Sea monsoon[73,74,99]. However, given the short observational record, it is not clear whether and to what extent these changes are attributable to greenhouse warming, and whether they will continue, necessitating the use of climate models.

Simulating IOD dynamics and characteristics

These observed processes and characteristics are often difficult to correctly simulate in climate models. Indeed, there are persistent model biases across multiple model generations (including CMIP6) in the simulation of the climatological tropical Indian Ocean[27,100–102]. For example, the equatorial climatological easterlies are overly strong, the thermocline overly shallow, and SSTs too cold over the eastern EIO (Supplementary Fig. 3). These mean state biases could affect the simulation of IOD dynamics and characteristics, causing uncertainty when assessing the future evolution of the IOD. We next discuss model simulations of these characteristics and their biases.

Simulated processes of IOD life cycle

Simulation of basic IOD characteristics includes correct seasonality, skewness and amplitude. The majority of models are able to simulate IOD maturity in austral spring, but there are differences from observations. For example, the IOD peaks in October in observations, but in November and September in the ensemble of CMIP5 and CMIP6 models, respectively[103]. In contrast, many models cannot simulate negative eastern EIO SST skewness — the greater amplitude of cold eastern EIO SST anomalies during pIOD compared to warm eastern EIO SST anomalies during nIOD — with 19 of 24 selected models (chosen on the basis of simulated IOD seasonality and negative eastern EIO SST skewness) simulating skewness that is too small (Fig. 2a). IOD amplitude is also biased, as demonstrated by 17 of the 24 selected models exhibiting DMI variability that is overestimated compared to observations.

Dynamical and thermodynamical feedbacks also exhibit large spread among models. Relative to observations, the wind response to SST feedback (Ekman pumping) tends to be underestimated in about 90% of models (Supplementary Fig. 4a) and the thermocline response to wind overestimated in about 70% of models in JJA and SON (Supplementary Fig. 4b); by contrast, the multi-model ensemble mean of thermocline feedback is close to the observed value and exhibits no clear systematic bias (Supplementary Fig. 4c). There is a strong relationship of thermocline feedback with DMI amplitude, reinforcing its dominant role in driving IOD variability. The nonlinear advection feedback is also reasonably represented (Fig. 2b), exhibiting a high inter-model correlation with DMI amplitude. Moreover, the majority of CMIP6 models display a relationship in which an increased downward net heat flux into the ocean is associated with cold SST anomalies over the eastern EIO, which encapsulates the net heat flux from the negative SST–cloud–radiative and the positive wind–evaporation–SST feedbacks (Supplementary Fig. 4d); therefore, during a pIOD event, the effect of reduced cloud cover in response to anomalous surface cooling overwhelms the wind–evaporation–SST feedback in the eastern EIO, although the modelled net negative feedback is overall weaker than the observed value in about 70% of models (Supplementary Fig. 4d).

The asymmetry in the strength of the feedbacks between pIOD and nIOD is generally underestimated, leading to weaker skewness[104]. In observations, the thermocline feedback is stronger during pIOD events[53,55,57,105] as the climatologically deep mean thermocline in the eastern EIO is more sensitive to easterly wind anomalies, which shoal it. The shoaling, in turn, brings cool deep water closer to the surface, further cooling the cold SST anomaly and enabling a pIOD to develop. In climate models, however, the overly shallow mean eastern EIO thermocline increases the sensitivity of the thermocline variability to westerly anomalies that are conducive to warm anomalies, reducing the amplitude asymmetry. As such, the thermocline feedback asymmetry exhibits a strong negative inter-model relationship with eastern EIO SST skewness (Supplementary Fig. 5a). The nonlinear advection feedback, which is reasonably simulated, also contributes to the skewness as it dampens warm SST anomalies but reinforces cold SST anomalies[6,49,52,58] (Supplementary Fig. 5b).

Simulated major IOD triggers

Climate models capture many factors that trigger and modulate IOD variability, including ENSO and the monsoon, although their linkage could be underestimated relative to the available observations. The coherence between ENSO and the IOD (the tendency for a pIOD to co-occur with El Niño development over austral winter and spring, and an nIOD with La Niña) is a robust feature in most climate models[103,106,107]. Their linkage is highlighted by a strong inter-model relationship between ENSO and IOD amplitudes[6,103,108,109]. However, the strength of ENSO–IOD coherence varies greatly across models and tends to be slightly weaker than observed, with 14 of 24 selected models exhibiting an underestimation (Fig. 2c). Various factors could contribute to this weaker relationship: the relatively higher occurrence of IOD events independent of ENSO in models[103], and the tendency for IOD events to be simulated the year after an El Niño owing to biases in ENSO oceanic teleconnections associated with crude representation of the complex maritime continent topography[109].

Monsoonal triggers of the simulated IOD also tend to be underestimated. In particular, 19 of 24 selected models display a weaker relationship than observations, probably related to the problematic simulation of monsoon onset process[71,110] (Fig. 2c). Other IOD-modulating factors such as Pacific decadal variability also tend to be underestimated by climate models in refs. 111,112, but the observational records are too short to confirm this, particularly when considering that the amplitude of simulated decadal variability is comparable to palaeo estimates[113].

Simulated IOD diversity

As with other factors, CMIP6 models tend to under-represent IOD event diversity. Event diversity is related to the nonlinear relationship between the first and second principal components of equatorial SSTs, measured as α. The strength of the nonlinear advective feedback which underpins IOD asymmetry tends to increase with α (Fig. 2d). Models with a larger

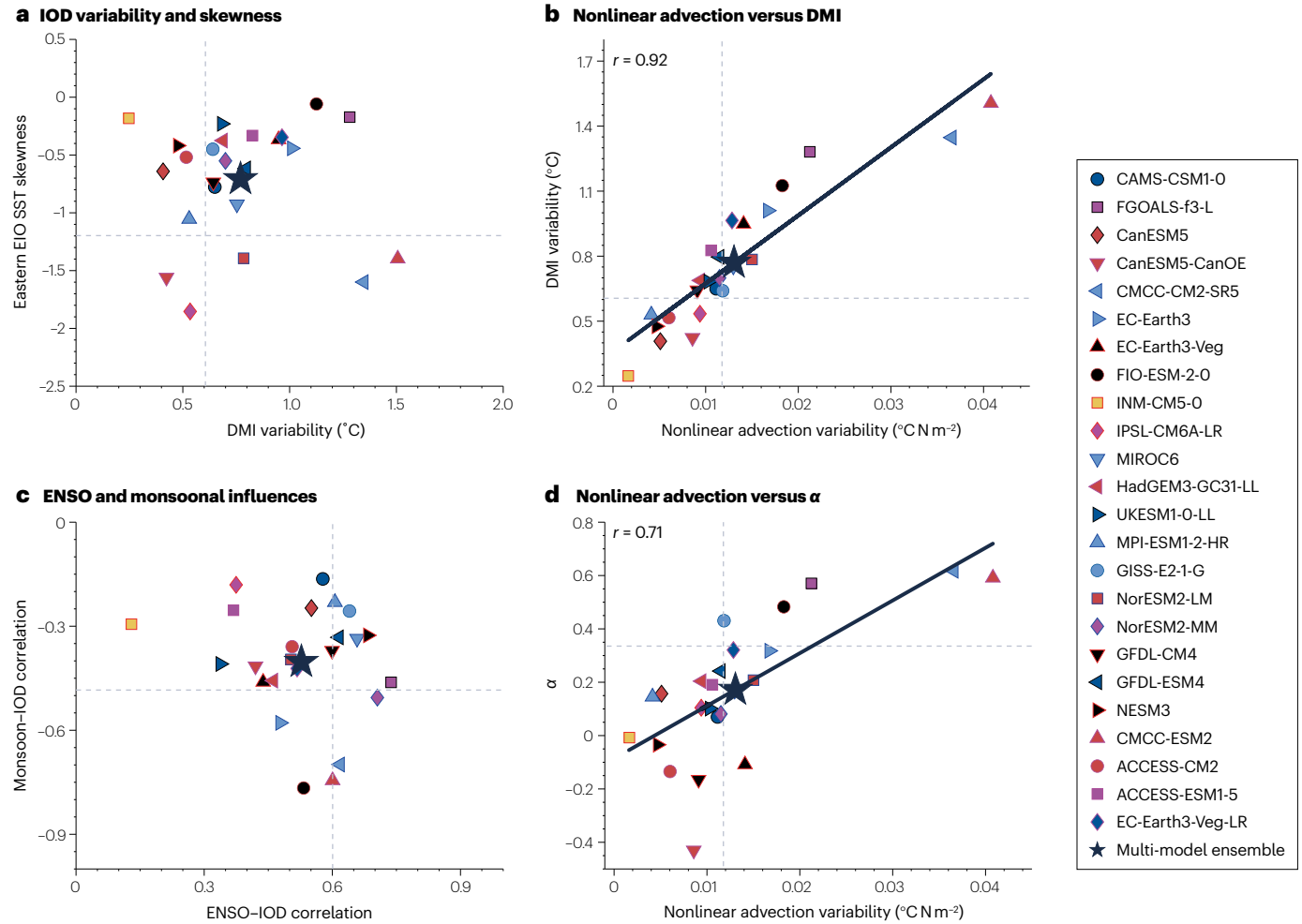

Fig. 2 | Simulated twentieth-century Indian Ocean Dipole characteristics. **a**, Inter-model spread in September–November (SON) dipole mode index (DMI) variability and SON eastern equatorial Indian Ocean (EIO) sea surface temperature (SST) skewness for 24 selected CMIP6 models and the multi-model ensemble. Dashed lines indicate observed values based on the multi-product mean. **b**, The inter-model relationship in nonlinear advection and DMI variability in SON. The correlation coefficient is indicated in the top left, and the line of best fit in black. **c**, Inter-model spread in couplings between the El Niño–Southern Oscillation (ENSO) and the Indian Ocean Dipole (IOD) and between the monsoon and the IOD. The ENSO–IOD and monsoon–IOD couplings are calculated as the correlation coefficients between the SON Niño3.4 index and the SON DMI, and between the central tropical Indian Ocean zonal wind anomalies in May and JJA DMI, respectively. **d**, As in **b**, but the inter-model relationship between variability in the nonlinear advection and α in SON; α is the nonlinear coefficient in the quadratic function between PC1 and PC2, that is, $PC2(t) = \alpha[PC1(t)]^2 + \beta PC1(t) + \gamma$. β and γ refer to the linear regression coefficient and noise, respectively. CMIP6 model biases include large IOD amplitude, weak skewness and weak monsoon–IOD coupling, but these are not as severe as once thought compared to more realistic products.

α value generally have a larger skewness in the S-index, but smaller skewness in the M-index (Supplementary Fig. 6). Among the 24 selected models, only 13 capture the nonlinear feature of pIOD with α greater than half of the observed value (Fig. 2d). This underrepresentation might be related to underestimated ENSO–IOD and monsoon–IOD relationships.

Moreover, models also show diverse ability in simulating the early-pIOD. Among 63 CMIP5 and CMIP6 models, only 25% of the models capture the features of the early-pIOD as observed, owing to deficiencies in the simulation of intraseasonal variability and convection[71,110]. This deficiency is presumably related to model simulation of the Asian monsoon which substantially influences the development of early IOD by modulating zonal wind along the tropical Indian Ocean[71].

Projected change in the IOD

Prior assessments of IOD changes are somewhat contradictory, suggesting increased IOD rainfall variability[6] but no consensus on DMI SST variability change[22,23]. However, selecting models in terms of their ability to simulate IOD diversity produces an inter-model consensus on changes in IOD amplitude and related feedbacks. We next discuss projected changes to the IOD.

Projected mean state changes

Changes in the tropical Indian Ocean mean state have a strong bearing on the IOD response to greenhouse warming[6,22,23,49]. In response to increased greenhouse gas emissions, the western EIO is projected to warm

faster than the eastern EIO[22–26], weakening the Walker circulation[24,114–116] and causing an equivalent change in mean rainfall between west and east (Fig. 3a). The enhanced west-minus-east SST gradient is associated with strengthened climatological easterlies along the tropical Indian Ocean, driving an west-to-east upward thermocline tilt[27] (Fig. 3b). The magnitude of such a pIOD-like warming pattern increases linearly with the global

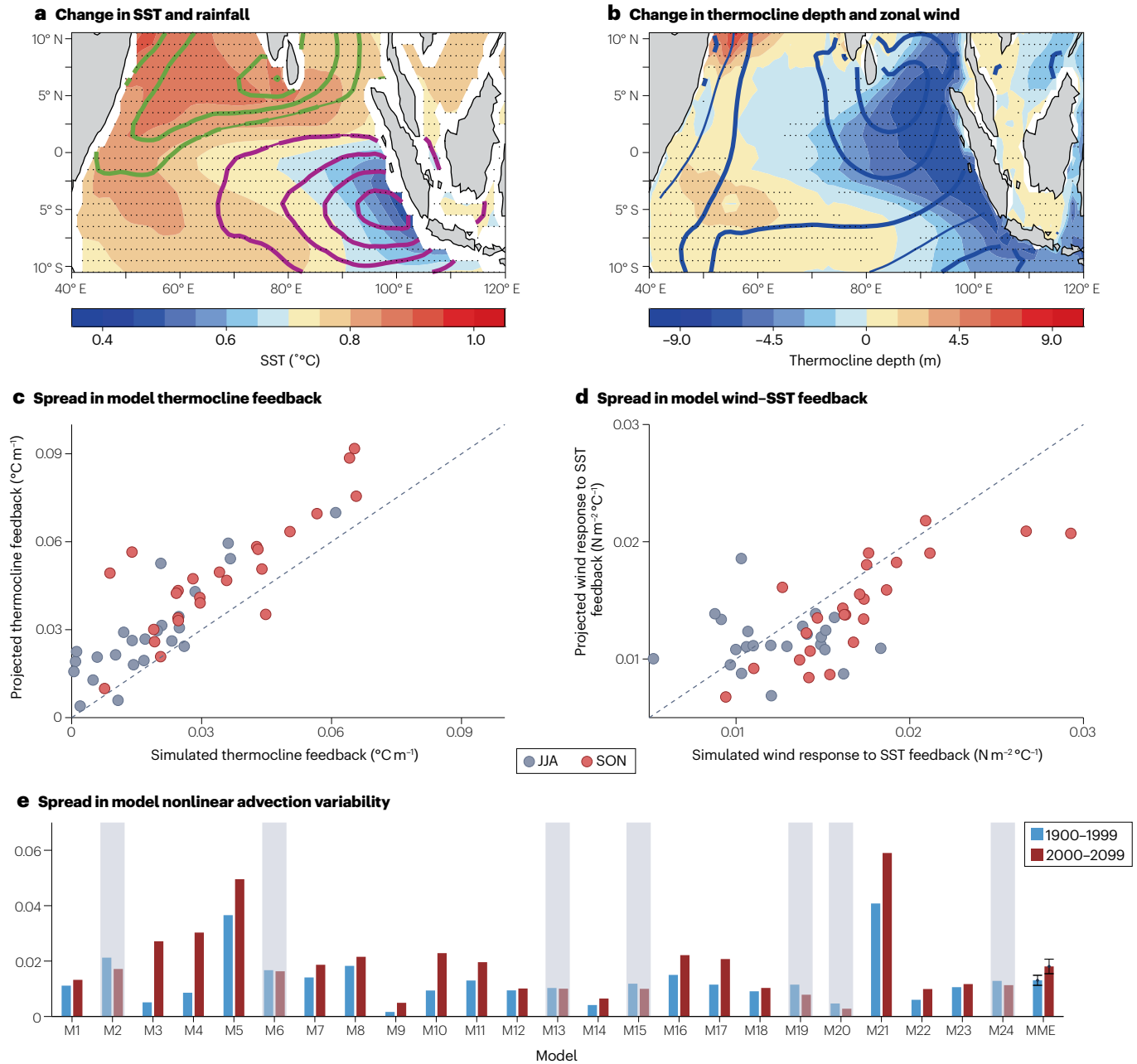

Fig. 3 | Projected changes in the mean state and feedbacks. a, Mean state change in sea surface temperature (SST; shading) and rainfall (contours) between the twentieth and twenty-first centuries in June–November for the multi-model ensemble. Green and purple contours represent positive and negative rainfall changes, respectively, drawn at intervals of 0.2 mm d^{-1} °C^{-1}. Dotted areas and thicker contours indicate statistically significant differences above the 90% confidence level, as revealed by a Student's *t* test. The projected changes have been scaled by the corresponding increase in global mean surface temperature in each model. **b**, As in panel **a**, but for projected changes in thermocline depth (shading) and surface zonal wind stress (contours). Blue contours represent easterly wind anomalies, drawn at intervals of 0.002 N m^{-2} °C^{-1}. **c**, The inter-model spread in the simulated and projected thermocline feedback for JJA (grey) and SON (orange). **d**, As in panel **c**, but for simulated and projected wind response to SST feedback. **e**, Comparison of SON nonlinear advection variability over the twentieth (blue bars) and twenty-first centuries (red bars) across different models and the multi-model ensemble (MME). Seven models that simulate a reduction in variance are greyed out. Error bars in the multi-model mean correspond to a one-standard-deviation range of the uncertainty based on a bootstrap method. Projected positive Indian Ocean Dipole (pIOD)-like mean state change leads to a stronger thermocline feedback and oceanic nonlinear advection, but weaker response of zonal winds to SST anomalies.

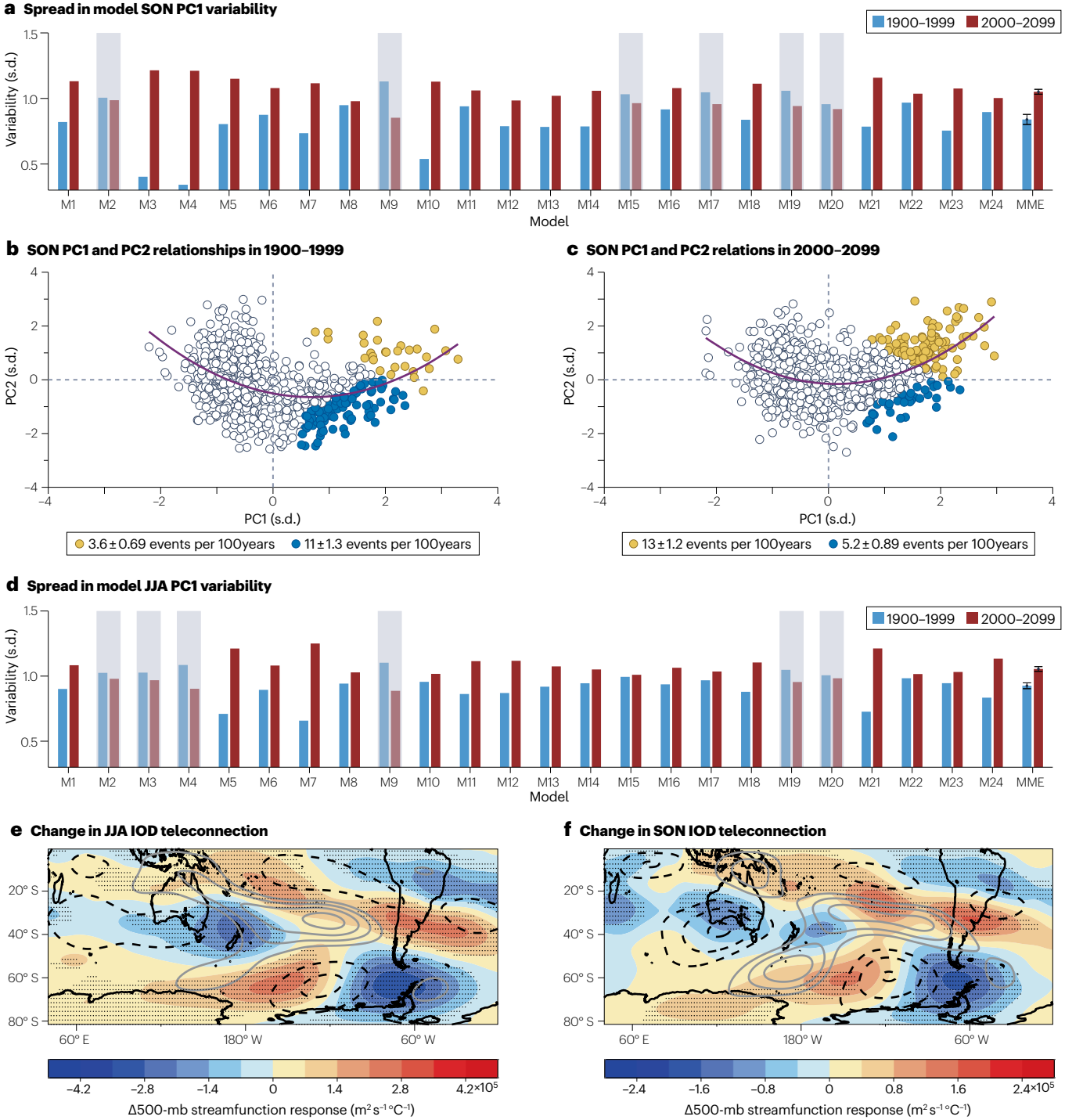

mean temperature rise[26]. In addition, the atmospheric air column is projected to become more stable as the troposphere warms faster than the surface[117,118], reducing zonal wind variability[22,23,119] (Supplementary Fig. 7a).

Projected changes in the feedbacks

Shifts in the mean state are expected to cause corresponding changes in IOD feedback processes. For instance, shoaling of the eastern EIO thermocline is conducive to a strengthened thermocline feedback[22,23,119], as found in more than 90% of selected models in JJA and SON (Fig. 3c). As a consequence of the more stabilized atmosphere and weakened zonal wind variability, there is also strong inter-model agreement for a weakening of the wind response to SST feedback[22,23] (Fig. 3d) and the thermocline response to wind feedback in SON (Supplementary Fig. 7b). These changes in the thermocline feedback

Fig. 4 | Projected changes in first principal mode SST variability, the strong- and moderate-pIOD regimes, and changes in IOD teleconnection. **a**, Simulated variability of the first principal component (PC1) of tropical Indian Ocean sea surface temperature (SST) during September–November (SON) in the twentieth (blue bars) and twenty-first century (red bars). Models that simulate a reduction in variance are greyed out. Error bars in the multi-model ensemble (MME) mean correspond to the one-standard-deviation range of the uncertainty based on a bootstrap method. **b**, Relationship between the first two principal component time series of equatorial (5°S–5°N, 40°E–100°E) Indian Ocean SST anomalies for the twentieth century based on the eight CMIP6 models that simulate at least half of the observed nonlinearity. Yellow dots denote strong-positive Indian Ocean Dipole (pIOD) events when the S-index ((PC1 + PC2)/√2) is >1.5 s.d., and blue dots denote moderate-pIOD events when the M-index ((PC1 − PC2)/√2) is >1.25 s.d. The frequency of strong and moderate events is noted, with a one-standard-deviation range indicating the uncertainties based on a bootstrap method. The purple line indicates a quadratic fit using PC1 and PC2 time series from the aggregate of the eight models. **c**, As in panel **b**, but for the twenty-first century. **d**, As in panel **a**, but for July–August (JJA) PC1 variability, with the models that simulate a reduction in variance greyed out. **e**, The twentieth-century IOD teleconnection pattern (contours), calculated as the 500-mb streamfunction regressed onto the JJA PC1 timeseries, and the difference in regression patterns between the twentieth and the twenty-first centuries (Δ; shading). Solid grey and dashed black lines indicate positive and negative streamfunction anomalies, respectively, from −9 to +9 × 10^5 m^2 s^{-1} $°C^{-1}$, at intervals of 3 × 10^5 m^2 s^{-1} $°C^{-1}$. Dotted areas indicate statistically significant differences above the 90% confidence level, based on a Student's *t* test. **f**, As in panel **e**, but for SON. There is inter-model consensus on a projected increase in IOD variability in austral winter and spring with a correspondingly stronger teleconnection. The increase in IOD variability translates to a decreasing frequency of moderate-pIOD but an increasing frequency of strong-pIOD and early-pIOD.

and wind response to zonal SST gradient offset each other, leading to muted changes in DMI SST variability[22,23]. In addition, faster warming in the west compared to the east means that there is an easterly wind trend in the mean state change and that the centre of atmospheric convection is easier to move westwards; as such, a smaller perturbation is required to generate the same size of easterly anomalies, conducive to nonlinear advection feedback in the twenty-first century[6,49] (Fig. 3e). Moreover, there is an increase in thermal damping as the background SST increases (Supplementary Fig. 7c).

Increased strong pIOD rainfall

Based on rainfall anomalies, future pIOD events are anticipated to become more extreme. This process occurs even if IOD SST variability does not change. Namely, the pattern of projected SST warming facilitates the movement of atmospheric convection to the west, with an increase in pIOD events characterized by anomalously higher rainfall in the western Indian Ocean and eastern African countries[6,102]. Feedback processes also contribute to these changes: the westward movement of convection moves initial cold and dry anomalies in the east westward; these push easterly anomalies and the western Indian Ocean convergence further toward Africa; corresponding equatorial upwelling and the westward oceanic current increase nonlinear advection feedback; cold and dry anomalies are amplified in the east, reinforcing a strong pIOD.

These increases are apparent across several generations of models. For instance, an ensemble of CMIP5 models that are selected following similar model selection criteria reveal a 150% increase in the frequency of such strong rainfall pIOD events (from 5.8 to 15.9 events from the twentieth to twenty-first centuries) under the Intergovernmental Panel on Climate Change (IPCC)'s Representaive Concentration Pathway (RCP) 8.5 (ref. 6; in RCP8.5, emissions continue to rise throughout the twenty-first century). Selected CMIP6 models suggest slightly stronger changes, projecting a shift from 3.6 to 17.0 events per 100 years under the IPCC's Shared Socioeconomic Pathways (SSPs) 5-8.5 (SSP5-8.5 have very high greenhouse gas emissions; Supplementary Figs. 8a and b). The evolution of greenhouse gas emissions, however, is important for the trajectory of IOD changes; CMIP5 models forced with RCP2.6 (very stringent reduction in carbon dioxide emissions) indicate that strong rainfall pIOD frequency stops increasing at approximately 2050 when the global mean temperature stabilizes[26].

Increased strong-pIOD and reduced moderate-pIOD

Simulated IOD SST anomaly centres are vastly different across models, meaning that any assessment should be based on the variability centre unique to each model[120], as represented by the dominant principal component. Averaged across all events, IOD SST variability tends to increase under greenhouse warming. For CMIP6, there is inter-model agreement on the projected changes in the first principal mode of SON SST variability from the twentieth to twenty-first century; 18 out of the 24 models project an increase, an inter-model agreement that is greater than when the DMI is used (Fig. 4a and Supplementary Fig. 8c).

The response of the average pattern does not reflect the response of all types of pIOD event, but encompasses an increase in strong-pIOD (S-index) and a decrease in moderate-pIOD (M-index), dominated by cool anomalies in the east but by warm anomalies in the west, respectively (Fig. 1d). The majority of models perform poorly in simulating the distinct anomaly centres of moderate- and strong-pIOD, with only 15 CMIP5 and five of the then-available CMIP6 models capturing at least 50% of observed regimes[49]. Those models indicate a 22% increase in SST variability of the strong-pIOD regime and a 15% decrease in SST variability of the moderate-pIOD regime[49]. Findings are broadly similar when using only CMIP6 models that meet the same criterion: the S-index amplitude increases by 23.2% (strong-pIOD events increase in frequency from 3.6 to 13.0 events per 100 years), while the M-index amplitude decreases by 13.6% (moderate-pIOD events decline in frequency from 11.0 to 5.2 events per 100 years) (Fig. 4b,c). These changes are underpinned by strong inter-model agreement.

Increased early-pIOD

In addition to a projected increase in the frequency of strong-pIOD, early-pIOD events are also expected to become more frequent. While not all models are able to reproduce the characteristics of observed early-pIOD events, in part because of a poor simulation of the monsoon onset process[110], six CMIP5 and ten CMIP6 models perform similarly to observations. 75% of these models simulate an increase in early-pIOD events under SSP5–8.5; their frequency rises 73% from 1.90 events every 31 years in the beginning of the twenty-first century to 3.28 events in 31 years at the end of the century[71]. The increase is underpinned by a stronger thermocline feedback in JJA (Fig. 3c) and an early summer monsoon onset in May[71,121]. Consistently, JJA SST variability associated with the IOD (PC1) increases in 18 of 24 models, and with statistical significance in the multi-model ensemble (Fig. 4d).

Intensification of teleconnections

Although there is seemingly consensus on changing IOD variability, potential changes in their teleconnections remain little explored[122]. However, several teleconnection changes can be inferred from the changes in the mean state and in IOD variability. First, sensitivity of rainfall anomalies to the IOD would increase even if IOD SST variability does not change[6]; this change occurs as a result of the SST warming pattern, an increase in atmospheric moisture[23,123] and associated enhancement in evaporation. Second, the overall impact of any teleconnections will increase, given the intensification of circulation anomalies from the projected increase in IOD variability. A stronger tropical response will drive more extreme short-rain season floods in eastern African countries but more severe drought over Indonesia[122]. The stronger extratropical response (Fig. 4e,f), which features stronger high pressure south of Australia[13], will lead to more severe drought over Australia. Such exacerbated impacts are expected in regions affected by downstream anomaly centres, such as Chile and southeast South America[92]. The impact would be particularly extreme during future strong-pIOD events in SON given that increased IOD variability arises from increased SST variability associated with the strong-pIOD regime. In addition, during future moderate-pIOD events, the reduced impact associated with the weaker circulation anomalies is compensated by the increased sensitivity to the mean state changes.

Bringing these collective changes in IOD together, it can be inferred that strong-pIOD variability in rainfall and SST anomalies will increase by 2100 under continued greenhouse warming. Similarly, early-pIOD SST variability will continue to increase. In contrast, moderate-pIOD SST variability will tend to decrease.

Factors influencing IOD projections

Understanding the dynamics behind the projected IOD changes is essential to reduce uncertainties. We next discuss the shift in the mean state, which has strong bearing on the IOD projection, as well as the influencing factors of ENSO, the monsoon, internal variability and the mean state biases.

Impacts from mean state change

Increased variability of strong-pIOD (represented by the S-index) is underpinned by faster warming in the west compared to the east[6,49], in turn, linked to a weakened Walker circulation[24,28,114–116]. The associated strengthened easterlies and westward shift of the atmospheric convection centre mean that a smaller perturbation is required to generate the same size of easterly anomalies, conducive to strengthening of nonlinear advection feedback, with a strong inter-model agreement (Supplementary Fig. 9a) (refs. 6,49). The reduction in moderate-pIOD variability (represented by the M-index) is supported by a more stable atmosphere because of a faster warming in the lower troposphere than the surface, driving a reduction in zonal wind response to SST feedback and, therefore, in zonal wind variability (Supplementary Fig. 9b). The decrease in the easterly wind anomalies limits Ekman pumping, which drives warm anomalies of the moderate-pIOD[49].

Impacts from changes in ENSO and monsoon

Present-day relationships between ENSO and the IOD imply that any projected changes in the IOD might arise from related changes in ENSO. Specifically, models with stronger ENSO variability tend to simulate greater IOD variability in the current climate[6,103,108,109]. Given that most models project an increase of CP- and EP-ENSO variability under greenhouse warming[120,124,125], it is possible that projected increases in IOD variability are forced by changes in ENSO–IOD coupling. However, the absence of inter-model consensus on projected ENSO–IOD coupling (Fig. 5a) suggests that IOD changes are unlikely to occur owing to changes in ENSO[6,49,126].

Likewise, a change in monsoon–IOD coupling is also expected to contribute to IOD changes. Despite the poorly simulated Asian monsoon and its onset in many CMIP6 models[71,127,128], monsoon–IOD coupling is projected to intensify under anthropogenic warming with strong inter-model agreement[71]. Indeed, the correlation between monsoon onset (as represented by May CTIO zonal wind anomalies) and the JJA IOD index (PC1) becomes more negative in the majority of models (Fig. 5b). This change is consistent with more frequently simulated early-pIOD events[71] and therefore increased austral winter IOD variability (Fig. 4d) (ref. 126), given that the Asian monsoon is their main driver.

Internal variability and mean state biases

Internal variability is one main source of the uncertainty in climate projections[129]. Using a large ensemble of simulations from a single climate model in which the only difference is the initial conditions with small perturbations, the spread of IOD amplitude change caused by internal variability can reach up to 40% of the inter-model spread of the CMIP5 multi-model ensemble[129]. The spread can be driven by ENSO[129], or the mean eastern EIO thermocline depth[130], which is different across experiments. To minimize the influence from internal variability and maximize the climate change signal, a 'model democracy' approach[131] is often used to assess the inter-model consensus in the projected changes, which uses one experiment from each model to avoid dominance by models with many experiments; comparing two century-long periods could also help. However, the difference might still contain a component induced by internal variability[130].

Common mean state biases in the tropical Indian Ocean persist[29,132,133] and could modulate IOD projections. Generally, such biases are conducive to an overly strong Bjerknes positive feedback giving rise to greater IOD amplitude[100,101]. Accordingly, the projected frequency increase in strong-pIOD events could be overestimated[101,134]. However, a systematic inter-model relationship between the projected change in such strong-pIOD and biases in the thermocline implies that the shallow thermocline bias inhibits further thermocline shallowing, suggesting an underestimation in the projected frequency increase[27,55,102]. Indeed, the majority of models tend to underestimate their projected increase in strong-pIOD SST variability and frequency[27,102] (Fig. 5c).

Although the projected change in IOD variability is primarily determined by mean state changes[6,26,44,49], changes in ENSO and Asian monsoon also contribute. In addition, projection continues to be uncertain owing to internal variability and model biases.

Palaeoclimatic perspectives

The brevity of reliable SST observations and climate model biases[135] hampers our understanding of the IOD, contributing to the uncertainties of its changing behaviour[136,137]. Palaeoclimate data from a range of proxy types (and often interpreted alongside palaeoclimate simulations) offer an additional stream of evidence with which to assess IOD variability in a warming climate, and include: coral and fossil coral records to reconstruct IOD variability since the mid-1800s[138] and further back in time[33,44,139], respectively; marine sediment cores to reconstruct century- to millennial-scale changes in tropical Indian Ocean mean SST[140–142]; isotopic analysis of individual foraminifera in marine sediments to reconstruct interannual SST variability during the Last

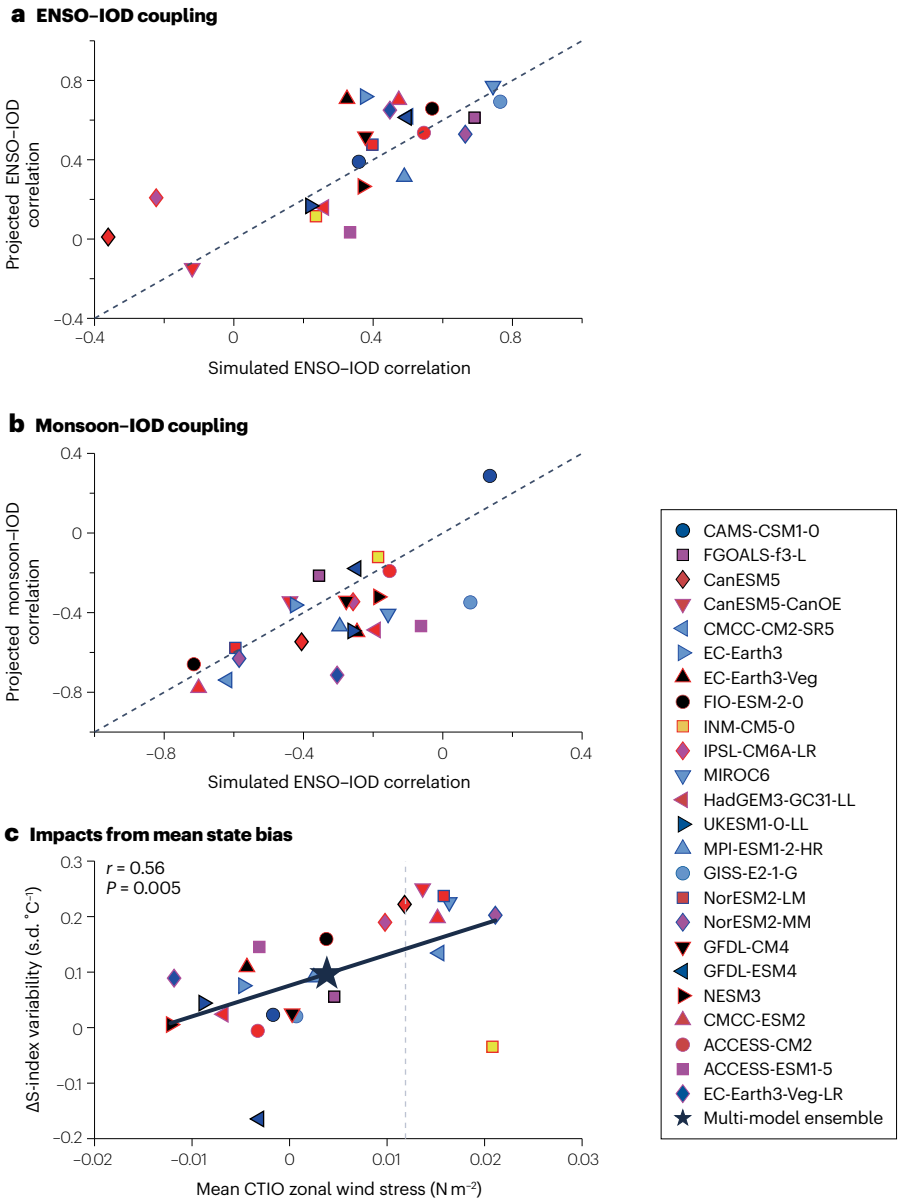

Fig. 5 | Projected changes in ENSO–IOD and monsoon–IOD couplings, and impacts of mean state bias on the IOD changes. a, Inter-model spread in simulated and projected coupling between El Niño–Southern Oscillation (ENSO) and the Indian Ocean Dipole (IOD) for the selected CMIP6 models. **b**, As in panel **a**, but for monsoon–IOD coupling. **c**, The inter-model relationship between twentieth century climatological mean central tropical Indian Ocean (CTIO) zonal wind stress and projected S-index sea surface temperature (SST) variability changes (Δ) across the selected CMIP6 models. The dashed vertical line indicates the observed climatological mean CTIO zonal wind stress. The correlation coefficient (*r*) and *p* value are indicated in the top left, and the line of best fit in black. Although there is no inter-model consensus on changes in ENSO–IOD coupling, monsoon–IOD coupling intensifies under greenhouse warming, and overly weak westerly winds along the equator potentially reduce the increase in strong-pIOD.

Glacial Maximum[143]; and lake and marine sediment leaf wax isotopes to reconstruct hydroclimate changes linked to the Indian Ocean Walker circulation[144,145].

These palaeoclimate data indicate an enhanced frequency and magnitude of pIOD events[138]. In particular, discontinuous time slices over the past millennium reveal only ten strong pIOD events, four of which occurred after 1960 (ref. 44). This change coincides with a shift to a more pIOD-like mean state[135,138]. If current trends continue, as suggested by climate projections[6,49,135], then the frequency of pIOD events will imminently emerge above the range of natural variability over the last millennium (Fig. 6a). Nevertheless, evidence of strong events during the seventeenth century suggests that the magnitude of IOD variability could remain within the bounds of natural variability. For instance, coral data identifies an event in around 1675 that was around 27–40% stronger than the extreme 1997 and 2019 events (Fig. 6b,c) – the largest events in the instrumental record[44].

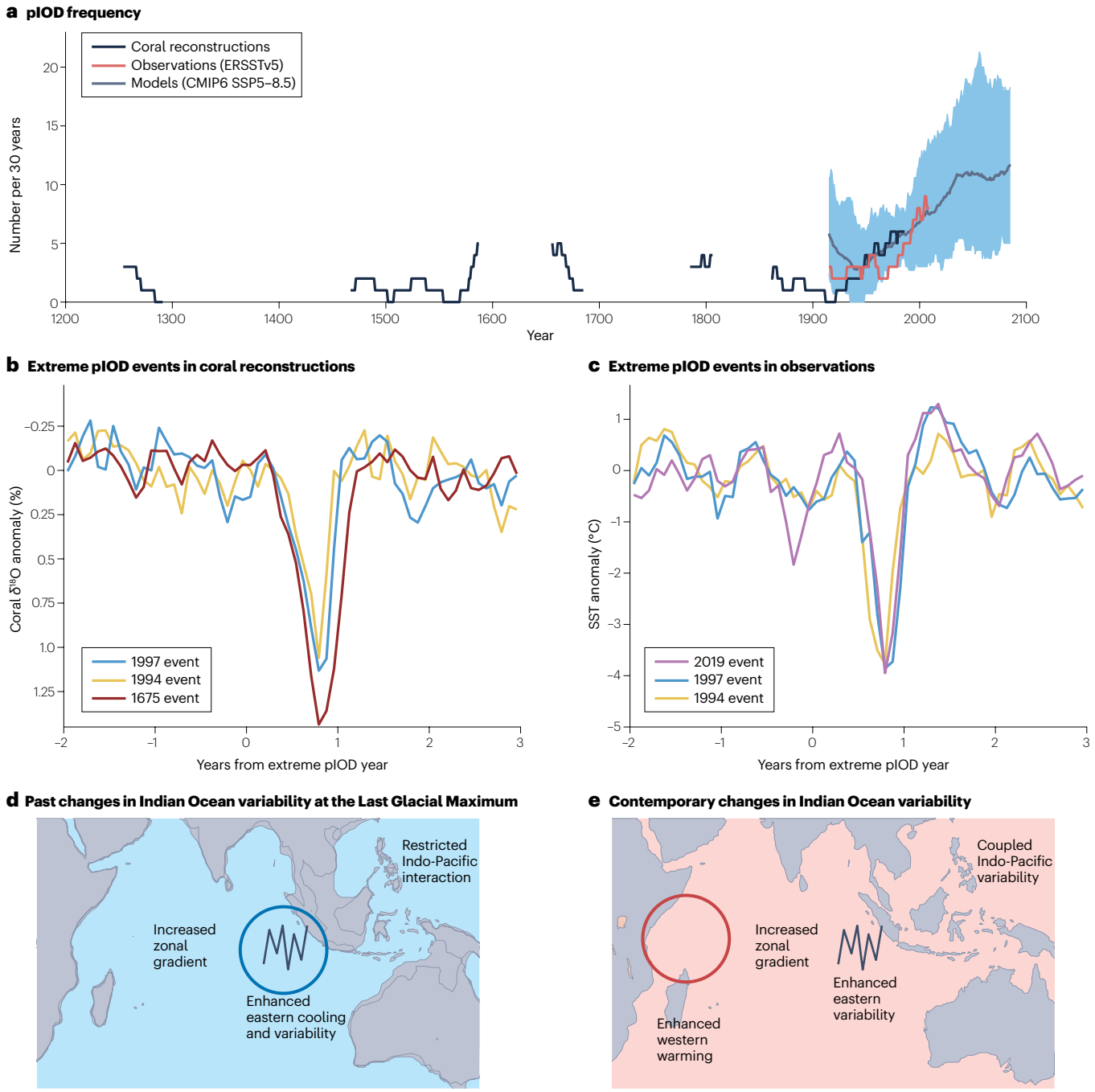

Fig. 6 | Past, present and future context for the IOD. a, Frequency of positive Indian Ocean Dipole (pIOD) events using coral data in the southern Mentawai Islands (black)[44,135], sea surface temperature (SST) observations in the same location (orange)[164] and modelled SST averaged over the eastern pole (grey line is the ensemble mean, shading is the 5–95% range across the 24-member ensemble). **b**, Coral $\delta^{18}O$ anomalies at 3 °S, 100 °E[44,135] preceding and following extreme pIOD events. **c**, As in panel **b**, but for observed SST anomalies[38]. **d**, Schematic of Indian Ocean mean state and eastern IOD variability changes during the Last Glacial Maximum. **e**, As in panel **d**, but contemporary changes. Palaeoclimate data indicate that a far stronger pIOD is possible, particularly in the eastern pole where SST variability is projected to increase substantially, and that an increase in IOD variability is accompanied by a strengthening in the west-minus-east mean SST gradient.

Times of enhanced IOD variability, as exhibited post-1960 and during the Last Glacial Maximum, related to periods of an enhanced west-minus-east SST gradient owing to faster warming over the western EIO than the eastern EIO[135] (Fig. 6d,e). Indeed, during the Last Glacial Maximum, there was a near-doubling of interannual variability in the upper-ocean mixed layer of the eastern IOD upwelling region[143].

An increase in the west-minus-east SST gradient resulted from restricted Indonesian throughflow of warm waters from the western Pacific into the Indian Ocean and, therefore, enhanced eastern EIO cooling, altering atmospheric convection over the exposed Sunda and Sahul shelves[142] (Fig. 6d). Accordingly, evidence of the mean state impact on IOD variability strengthened and more frequent pIOD events suggest that future IOD impacts could be even more extreme than experienced in the instrumental record.

Palaeoclimate data further demonstrates a close coupling of the magnitude of interannual IOD variability with ENSO and the monsoon. During the last millennium, this ENSO–IOD connection amounts for 45% of the shared variance[44], with multi-decadal modulation of the IOD and ENSO variability closely following changes in the zonal SST gradient across the equatorial Pacific Ocean[146]. Prior to the fifteenth century, IOD and ENSO variability were reduced by around 30% compared with their 1961–1990 climatological means, and the equatorial Pacific had an enhanced west-minus-east equatorial SST gradient[44]. During the mid-Holocene, when ENSO variance was muted[147,148] but the Asian monsoon was strong[33,149], there were several strong pIOD events that exceed historical events in amplitude[33,139], further enhancing the potential for stronger future pIOD events than those observed since 1900.

Palaeoclimate data provide evidence that the frequency of pIOD fluctuates vastly, with the tropical Indian Ocean harbouring stronger pIOD events than the strongest in observation. However, under continued greenhouse forcing, twenty-first-century IOD SST variability will probably increase above the maximum natural variability for the last millennium.

Summary and future perspectives

Among models that can simulate the amplitude asymmetry between pIOD and nIOD[49,71,121], there is an emerging consensus toward enhanced IOD SST variability in austral winter and spring in the future. These changes translate to more frequent strong-pIOD and early-pIOD events (with a corresponding intensification of the tropical circulation response, extratropical teleconnections and thereby rainfall anomalies), but less frequent moderate-pIOD events (with no obvious change in the associated rainfall anomalies because rainfall sensitivity to SST anomalies is increased owing to the mean state change). The projected increase in strong-pIOD SST and rainfall variability is consistent with palaeoclimatic evidence that suggests that IOD variability has increased since the 1960s compared with past centuries, and that IOD variability amplitude tends to increase with an intensified west-minus-east equatorial

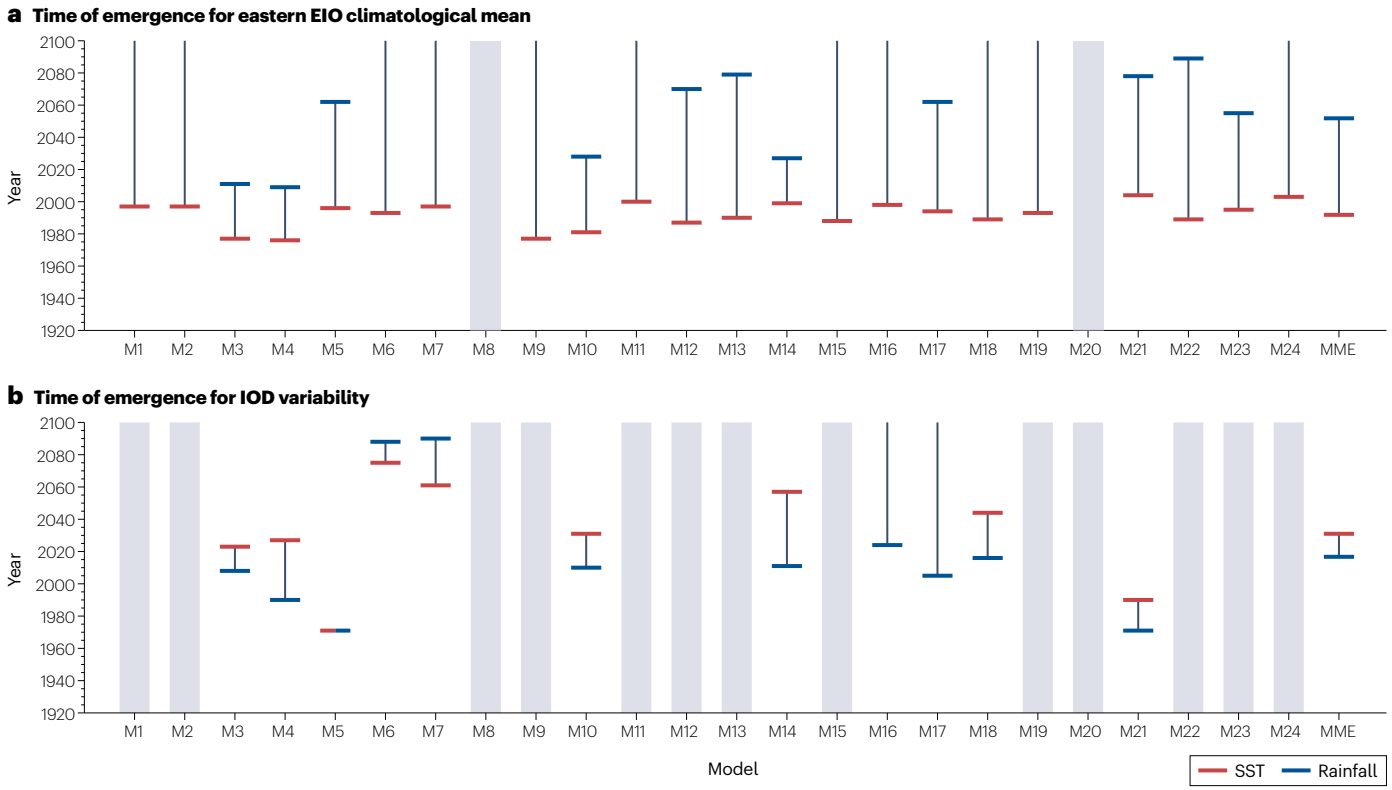

Fig. 7 | Time of emergence of climate change signals in the tropical Indian Ocean. a, The time of emergence (ToE; the year when anthropogenic signals emerge from noise) of annual mean sea surface temperature (SST; red) and rainfall (blue) over the eastern equatorial Indian Ocean region for 24 selected CMIP6 models and the multi-model ensemble (MME) mean. Signals are obtained by regressing annual mean time series in each grid point onto a smoothed version of the global mean (60° S–60° N) by fitting a fourth-order polynomial[150]. Noise is taken from the corresponding piControl using all available data. ToE is defined as the year when the signal-to-noise ratio exceeds +1 for SST but is below −1 for rainfall. **b**, The ToE for interannual variability in SON PC1 based on both SST (red) and rainfall (blue). Signals for variability are obtained by calculating variability in a 71-year running window from the start of the piControl simulation to the end of the twenty-first century. Noise is defined as one standard deviation of the piControl timeseries. The ToE for variability is defined as when the warming-induced signal-to-noise ratio first exceeds +2 and remains above +2 for both SST and rainfall variability[151]. Models that do not have ToE before 2100 for both SST and rainfall are greyed out. ToE for mean SST is earlier than ToE for mean rainfall but the reverse is true in terms of IOD SST and rainfall variability.

zonal SST gradient on long timescales[44] and with a strengthened Asian monsoon[33].

However, there is large uncertainty in IOD projections, as characterized by large inter-model spread. This spread highlights persistent (but varying) biases in the mean state (overly strong west-minus-east SST gradient, a too-steep thermocline tilt towards the east, and overly strong JJA and SON easterlies) and subsequent effects on IOD feedbacks, as well as the impact of internal variability (for example, the subtropical Indian Ocean Dipole[75–77] and the multidecadal Pacific Decadal Oscillation[80,83–85]). How to improve the simulation of these factors and their corresponding impact on IOD projections is unknown, but the use of large ensemble experiments might address key issues, including whether the observed IOD variability has already been affected by greenhouse warming.

Indeed, the use of large ensemble experiments allows the quantification of the time of emergence (ToE) — when anthropogenic changes emerge from the background noise of internal variability[124,150,151]. Under a high-greenhouse-gas-emission scenario, the ToE for mean eastern EIO SST is earlier than mean eastern EIO rainfall (Fig. 7a); mean SST signals have already emerged, whereas mean rainfall signals are projected to occur by 2050 when averaged across all models. In contrast, changes in IOD-related rainfall variability emerge earlier than for SST variability when averaged across the models (Fig. 7b), but are not expected to emerge before 2100 for either variable in more than half the models. A systematic investigation of the detectability of IOD changes is needed. For example, the IOD response might be nonlinear, such that beyond 2100 the reduction in wind variability from the more stable atmosphere could reverse the increase in variability of the S-index, leading to decreased strong-pIOD events[152]. The reversal could be a reason for the lack of the ToE.

In general, progress is lacking in improving model representation of the IOD and, therefore, in understanding IOD changes in the future, especially in comparison to ENSO. For instance, the role and simulation of nonlinear feedbacks[120,124], the influence of mesoscale and sub-mesoscale eddies in the heat budget[153–157], and subsequent impacts on the high latitudes[91,158–160] are all better developed and understood for ENSO than for the IOD.

Therefore, international efforts like those devoted to ENSO projection research, for instance, the CLIVAR ENSO Task Team, the ENSO Metrics Team[161], and the ENSO Conceptual Model Working Group would offer effective pathways to fast-track progress and improve understanding of the mechanisms and their representation in climate models. Priorities include: enhanced collaboration between observationalists and modellers to accelerate improvement in simulation of the Indian Ocean climatological circulation, nonlinear feedbacks and IOD interactions with the monsoon and other modes of variability; an increased capacity to analyse available model outputs focusing on the impact of model biases on IOD future change and its rectification; a better understanding of the role of internal variability in projected IOD changes and the impact of a changing IOD on global climate; and an enhanced effort to examine the role of mesoscale and sub-mesoscale processes in IOD dynamics.

These efforts will improve our understanding of IOD dynamics, interactions with modes of variability outside the Indian Ocean, such as ENSO, and its representation in climate models, ultimately reducing uncertainty in projected IOD changes — essential for informing adaptation strategies for the affected communities. These advances will also benefit research on ENSO and other modes of climate variability under the framework of pan-tropical climate interactions, and will ultimately benefit society given the global socio-economic ramifications of these climate modes[162,163].

Published online: 30 July 2024

References

1. Saji, N., Goswami, B. N., Vinayachandran, P. & Yamagata, T. A dipole mode in the tropical Indian Ocean. *Nature* **401**, 360–363 (1999).
2. Webster, P. J., Moore, A. M., Loschnigg, J. P. & Leben, R. R. Coupled ocean–atmosphere dynamics in the Indian Ocean during 1997–98. *Nature* **401**, 356–360 (1999).
3. Murtugudde, R., McCreary, J. P. Jr & Busalacchi, A. J. Oceanic processes associated with anomalous events in the Indian Ocean with relevance to 1997–1998. *J. Geophys. Res. Atmos.* **105**, 3295–3306 (2000).
4. Shi, W. & Wang, M. A biological Indian Ocean Dipole event in 2019. *Sci. Rep.* **11**, 2452 (2021).
5. McMonigal, K. & Larson, S. M. ENSO explains the link between Indian Ocean Dipole and meridional ocean heat transport. *Geophys. Res. Lett.* **49**, e2021GL095796 (2022).
6. Cai, W. et al. Increased frequency of extreme Indian Ocean Dipole events due to greenhouse warming. *Nature* **510**, 254–258 (2014).
7. Hashizume, M., Terao, T. & Minakawa, N. The Indian Ocean Dipole and malaria risk in the highlands of western Kenya. *Proc. Natl Acad. Sci. USA* **106**, 1857–1862 (2009).
8. Hashizume, M., Chaves, L. F. & Minakawa, N. Indian Ocean Dipole drives malaria resurgence in East African highlands. *Sci. Rep.* **2**, 269 (2012).
9. Nicholson, S. E., Fink, A. H., Funk, C., Klotter, D. A. & Satheesh, A. R. Meteorological causes of the catastrophic rains of October/November 2019 in equatorial Africa. *Glob. Planet. Change* **208**, 103687 (2022).
10. Latif, M., Dommenget, D., Dima, M. & Grötzner, A. The role of Indian Ocean sea surface temperature in forcing East African rainfall anomalies during December–January 1997/98. *J. Clim.* **12**, 3497–3504 (1999).
11. Birkett, C., Murtugudde, R. & Allan, T. Indian Ocean climate event brings floods to East Africa's lakes and the Sudd Marsh. *Geophys. Res. Lett.* **26**, 1031–1034 (1999).
12. Cai, W., Cowan, T. & Raupach, M. Positive Indian Ocean Dipole events precondition southeast Australia bushfires. *Geophys. Res. Lett.* **36**, https://doi.org/10.1029/2009GL039902 (2009).
13. Cai, W., Van Rensch, P., Cowan, T. & Hendon, H. H. Teleconnection pathways of ENSO and the IOD and the mechanisms for impacts on Australian rainfall. *J. Clim.* **24**, 3910–3923 (2011).
14. Nur'utami, M. N. & Hidayat, R. Influences of IOD and ENSO to Indonesian rainfall variability: role of atmosphere–ocean interaction in the Indo-Pacific sector. *Proc. Environ. Sci.* **33**, 196–203 (2016).
15. Wang, G. & Cai, W. Two-year consecutive concurrences of positive Indian Ocean Dipole and central Pacific El Niño preconditioned the 2019/2020 Australian "black summer" bushfires. *Geosci. Lett.* **7**, 19 (2020).
16. Abram, N. J. et al. Connections of climate change and variability to large and extreme forest fires in southeast Australia. *Commun. Earth Environ.* **2**, 8 (2021).
17. van der Velde, I. R. et al. Vast CO_2 release from Australian fires in 2019–2020 constrained by satellite. *Nature* **597**, 366–369 (2021).
18. Saji, N. & Yamagata, T. Possible impacts of Indian Ocean Dipole mode events on global climate. *Clim. Res.* **25**, 151–169 (2003).
19. Chan, S. C., Behera, S. K. & Yamagata, T. Indian Ocean Dipole influence on South American rainfall. *Geophys. Res. Lett.* **35**, https://doi.org/10.1029/2008GL034204 (2008).
20. Bell, G. et al. Tropical cyclones — Atlantic basin, state of the climate in 2011. *Bull. Am. Meteor. Soc.* **98**, S108–S112 (2017).
21. Wood, K. M. et al. Factors affecting the 2019 Atlantic hurricane season and the role of the Indian Ocean Dipole. *Geophys. Res. Lett.* **47**, e2020GL087781 (2020).
22. Zheng, X.-T. et al. Indian Ocean Dipole response to global warming in the CMIP5 multimodel ensemble. *J. Clim.* **26**, 6067–6080 (2013).
23. Cai, W. et al. Projected response of the Indian Ocean Dipole to greenhouse warming. *Nat. Geosci.* **6**, 999–1007 (2013).
24. Vecchi, G. A. & Soden, B. J. Global warming and the weakening of the tropical circulation. *J. Clim.* **20**, 4316–4340 (2007).
25. Xie, S.-P. et al. Global warming pattern formation: sea surface temperature and rainfall. *J. Clim.* **23**, 966–986 (2010).
26. Cai, W. et al. Stabilised frequency of extreme positive Indian Ocean Dipole under 1.5 C warming. *Nat. Commun.* **9**, 1419 (2018).
27. Wang, G., Cai, W. & Santoso, A. Simulated thermocline tilt over the tropical Indian Ocean and its influence on future sea surface temperature variability. *Geophys. Res. Lett.* **48**, e2020GL091902 (2021).
28. Sharma, S. et al. Future Indian Ocean warming patterns. *Nat. Commun.* **14**, 1789 (2023).
29. Eyring, V. et al. Overview of the coupled model intercomparison project phase 6 (CMIP6) experimental design and organization. *Geosci. Model. Dev.* **9**, 1937–1958 (2016).
30. Izumo, T. et al. Influence of Indian Ocean Dipole and Pacific recharge on following year's El Niño: interdecadal robustness. *Clim. Dyn.* **42**, 291–310 (2014).
31. Chan, D., Kent, E. C., Berry, D. I. & Huybers, P. Correcting datasets leads to more homogeneous early-twentieth-century sea surface warming. *Nature* **571**, 393–397 (2019).
32. Gopika, S. et al. Aliasing of the Indian Ocean externally-forced warming spatial pattern by internal climate variability. *Clim. Dyn.* **54**, 1093–1111 (2020).
33. Abram, N. J. et al. Seasonal characteristics of the Indian Ocean Dipole during the holocene epoch. *Nature* **445**, 299–302 (2007).
34. Yang, K. et al. Oceanic processes in ocean temperature products key to a realistic presentation of positive Indian Ocean Dipole nonlinearity. *Geophys. Res. Lett.* **47**, e2020GL089396 (2020).

35. An, S.-I. et al. Main drivers of Indian Ocean Dipole asymmetry revealed by a simple IOD model. *npj Clim. Atmos. Sci.* **6**, 93 (2023).
36. Huang, B. et al. Extended reconstructed sea surface temperature, version 5 (ERSSTv5): upgrades, validations, and intercomparisons. *J. Clim.* **30**, 8179–8205 (2017).
37. Rayner, N. et al. Global analyses of sea surface temperature, sea ice, and night marine air temperature since the late nineteenth century. *J. Geophys. Res. Atmos.* **108**, https://doi.org/10.1029/2002JD002670 (2003).
38. Reynolds, R. W., Rayner, N. A., Smith, T. M., Stokes, D. C. & Wang, W. An improved in situ and satellite SST analysis for climate. *J. Clim.* **15**, 1609–1625 (2002).
39. Behringer, D. & Xue, Y. Evaluation of the Global Ocean Data Assimilation System at NCEP: the Pacific Ocean. In *Proc. Eighth Symp. on Integrated Observing and Assimilation Systems for Atmosphere, Oceans, and Land Surface* (Americal Meteorological Society, 2004).
40. Jackett, D. R., McDougall, T. J., Feistel, R., Wright, D. G. & Griffies, S. M. Algorithms for density, potential temperature, conservative temperature, and the freezing temperature of seawater. *J. Atmos. Ocean. Technol.* **23**, 1709–1728 (2006).
41. Giese, B. S. & Ray, S. El Niño variability in simple ocean data assimilation (SODA), 1871–2008. *J. Geophys. Res. Oceans* **116**, https://doi.org/10.1029/2010JC006695 (2011).
42. Zuo, H., Balmaseda, M. A., Tietsche, S., Mogensen, K. & Mayer, M. The ECMWF operational ensemble reanalysis–analysis system for ocean and sea ice: a description of the system and assessment. *Ocean. Sci.* **15**, 779–808 (2019).
43. Fischer, A. S., Terray, P., Guilyardi, E., Gualdi, S. & Delecluse, P. Two independent triggers for the Indian Ocean Dipole/zonal mode in a coupled GCM. *J. Clim.* **18**, 3428–3449 (2005).
44. Abram, N. J. et al. Coupling of Indo-Pacific climate variability over the last millennium. *Nature* **579**, 385–392 (2020).
45. Li, T., Wang, B., Chang, C. & Zhang, Y. A theory for the Indian Ocean Dipole–zonal mode. *J. Atmos. Sci.* **60**, 2119–2135 (2003).
46. Xie, S.-P., Annamalai, H., Schott, F. A. & McCreary, J. P. Structure and mechanisms of south Indian Ocean climate variability. *J. Clim.* **15**, 864–878 (2002).
47. Du, Y., Xie, S.-P., Huang, G. & Hu, K. Role of air–sea interaction in the long persistence of El Niño–induced north Indian Ocean warming. *J. Clim.* **22**, 2023–2038 (2009).
48. Du, Y. et al. Thermocline warming induced extreme Indian Ocean Dipole in 2019. *Geophys. Res. Lett.* **47**, e2020GL090079 (2020).
49. Cai, W. et al. Opposite response of strong and moderate positive Indian Ocean Dipole to global warming. *Nat. Clim. Change* **11**, 27–32 (2021).
50. Zhang, Y. & Du, Y. Oceanic Rossby waves induced two types of ocean–atmosphere response and opposite Indian Ocean Dipole phases. *J. Clim.* **35**, 3927–3945 (2022).
51. Ng, B., Cai, W., Walsh, K. & Santoso, A. Nonlinear processes reinforce extreme Indian Ocean Dipole events. *Sci. Rep.* **5**, 11697 (2015).
52. Wang, G., Cai, W., Yang, K., Santoso, A. & Yamagata, T. A unique feature of the 2019 extreme positive Indian Ocean Dipole event. *Geophys. Res. Lett.* **47**, e2020GL088615 (2020).
53. Hong, C.-C., Li, T. & Kug, J.-S. Asymmetry of the Indian Ocean Dipole. Part I: observational analysis. *J. Clim.* **21**, 4834–4848 (2008).
54. Cai, W. & Qiu, Y. An observation-based assessment of nonlinear feedback processes associated with the Indian Ocean Dipole. *J. Clim.* **26**, 2880–2890 (2013).
55. Ng, B., Cai, W. & Walsh, K. Nonlinear feedbacks associated with the Indian Ocean Dipole and their response to global warming in the GFDL–ESM2M coupled climate model. *J. Clim.* **27**, 3904–3919 (2014).
56. Cai, W., Hendon, H. H. & Meyers, G. Indian Ocean Dipolelike variability in the CSIRO Mark 3 coupled climate model. *J. Clim.* **18**, 1449–1468 (2005).
57. Ogata, T., Xie, S.-P., Lan, J. & Zheng, X. Importance of ocean dynamics for the skewness of the Indian Ocean Dipole mode. *J. Clim.* **26**, 2145–2159 (2013).
58. Nakazato, M., Kido, S. & Tozuka, T. Mechanisms of asymmetry in sea surface temperature anomalies associated with the Indian Ocean Dipole revealed by closed heat budget. *Sci. Rep.* **11**, 22546 (2021).
59. Hong, C. C., Lu, M. M. & Kanamitsu, M. Temporal and spatial characteristics of positive and negative Indian Ocean Dipole with and without ENSO. *J. Geophys. Res. Atmos.* **113**, https://doi.org/10.1029/2007JD009151 (2008).
60. Cai, W. et al. Pantropical climate interactions. *Science* **363**, eaav4236 (2019).
61. Wang, C. Three-ocean interactions and climate variability: a review and perspective. *Clim. Dyn.* **53**, 5119–5136 (2019).
62. Annamalai, H. et al. Coupled dynamics over the Indian Ocean: spring initiation of the zonal mode. *Deep. Sea Res. II* **50**, 2305–2330 (2003).
63. Zhao, Y. & Nigam, S. The Indian Ocean Dipole: a monopole in SST. *J. Clim.* **28**, 3–19 (2015).
64. Stuecker, M. F. et al. Revisiting ENSO/Indian Ocean Dipole phase relationships. *Geophys. Res. Lett.* **44**, 2481–2492 (2017).
65. Ashok, K., Guan, Z. & Yamagata, T. A look at the relationship between the ENSO and the Indian Ocean Dipole. *J. Meteorol. Soc. Japan. Ser. II* **81**, 41–56 (2003).
66. Behera, S. K. et al. A CGCM study on the interaction between IOD and ENSO. *J. Clim.* **19**, 1688–1705 (2006).
67. Yang, Y. et al. Seasonality and predictability of the Indian Ocean Dipole mode: ENSO forcing and internal variability. *J. Clim.* **28**, 8021–8036 (2015).
68. Lim, E.-P. & Hendon, H. H. Causes and predictability of the negative Indian Ocean Dipole and its impact on La Niña during 2016. *Sci. Rep.* **7**, 12619 (2017).
69. Sun, S., Lan, J., Fang, Y., Tana & Gao, X. A triggering mechanism for the Indian Ocean Dipoles independent of ENSO. *J. Clim.* **28**, 5063–5076 (2015).
70. Xiang, B., Yu, W., Li, T. & Wang, B. The critical role of the boreal summer mean state in the development of the IOD. *Geophys. Res. Lett.* **38**, https://doi.org/10.1029/2010GL045851 (2011).
71. Sun, S., Fang, Y., Zu, Y., Liu, L. & Li, K. Increased occurrences of early Indian Ocean Dipole under global warming. *Sci. Adv.* **8**, eadd6025 (2022).
72. Du, Y., Cai, W. & Wu, Y. A new type of the Indian Ocean Dipole since the mid-1970s. *J. Clim.* **26**, 959–972 (2013).
73. Zhang, Y. et al. Impact of the South China Sea summer monsoon on the Indian Ocean Dipole. *J. Clim.* **31**, 6557–6573 (2018).
74. Zhang, Y. et al. The relative roles of the South China Sea summer monsoon and ENSO in the Indian Ocean Dipole development. *Clim. Dyn.* **53**, 6665–6680 (2019).
75. Behera, S. K. & Yamagata, T. Subtropical SST dipole events in the southern Indian Ocean. *Geophys. Res. Lett.* **28**, 327–330 (2001).
76. Zhang, Y. et al. Indian Ocean tripole mode and its associated atmospheric and oceanic processes. *Clim. Dyn.* **55**, 1367–1383 (2020).
77. Huang, B. et al. Strengthened relationship between tropical Indian Ocean Dipole and subtropical Indian Ocean Dipole after the late 2000s. *Geophys. Res. Lett.* **48**, e2021GL094835 (2021).
78. Chen, P., Sun, B., Wang, H. & Zhu, B. Possible impacts of December Laptev sea ice on Indian Ocean Dipole conditions during spring. *J. Clim.* **34**, 6927–6943 (2021).
79. Izumo, T., Khodri, M., Lengaigne, M. & Suresh, I. A subsurface Indian Ocean Dipole response to tropical volcanic eruptions. *Geophys. Res. Lett.* **45**, 9150–9159 (2018).
80. Annamalai, H., Xie, S., McCreary, J. & Murtugudde, R. Impact of Indian Ocean sea surface temperature on developing El Niño. *J. Clim.* **18**, 302–319 (2005).
81. Tozuka, T., Luo, J.-J., Masson, S. & Yamagata, T. Decadal modulations of the Indian Ocean Dipole in the SINTEX-F1 coupled GCM. *J. Clim.* **20**, 2881–2894 (2007).
82. Nidheesh, A. et al. Natural decadal sea-level variability in the Indian Ocean: lessons from CMIP models. *Clim. Dyn.* **53**, 5653–5673 (2019).
83. Han, W. et al. Indian Ocean decadal variability: a review. *Bull. Am. Meteorol. Soc.* **95**, 1679–1703 (2014).
84. Krishnamurthy, L. & Krishnamurthy, V. Decadal and interannual variability of the Indian Ocean SST. *Clim. Dyn.* **46**, 57–70 (2016).
85. Dong, L. et al. The footprint of the inter-decadal Pacific oscillation in Indian Ocean sea surface temperatures. *Sci. Rep.* **6**, 21251 (2016).
86. Zhang, Y. et al. Strengthened Indonesian throughflow drives decadal warming in the southern Indian Ocean. *Geophys. Res. Lett.* **45**, 6167–6175 (2018).
87. Horel, J. D. & Wallace, J. M. Planetary-scale atmospheric phenomena associated with the Southern Oscillation. *Monthly Weather. Rev.* **109**, 813–829 (1981).
88. Hoskins, B. J. & Karoly, D. J. The steady linear response of a spherical atmosphere to thermal and orographic forcing. *J. Atmos. Sci.* **38**, 1179–1196 (1981).
89. Saji, N., Ambrizzi, T. & Ferraz, S. E. T. Indian Ocean Dipole mode events and austral surface air temperature anomalies. *Dyn. Atmos. Ocean.* **39**, 87–101 (2005).
90. Gillett, Z., Hendon, H., Arblaster, J., Lin, H. & Fuchs, D. On the dynamics of Indian Ocean teleconnections into the Southern Hemisphere during austral winter. *J. Atmos. Sci.* **79**, 2453–2469 (2022).
91. Li, X. et al. Tropical teleconnection impacts on Antarctic climate changes. *Nat. Rev. Earth Environ.* **2**, 680–698 (2021).
92. Cai, W. et al. Climate impacts of the El Niño–Southern Oscillation on South America. *Nat. Rev. Earth Environ.* **1**, 215–231 (2020).
93. Cai, W., Van Rensch, P., Cowan, T. & Hendon, H. H. An asymmetry in the IOD and ENSO teleconnection pathway and its impact on Australian climate. *J. Clim.* **25**, 6318–6329 (2012).
94. Endo, S. & Tozuka, T. Two flavors of the Indian Ocean Dipole. *Clim. Dyn.* **46**, 3371–3385 (2016).
95. Tozuka, T., Endo, S. & Yamagata, T. Anomalous Walker circulations associated with two flavors of the Indian Ocean Dipole. *Geophys. Res. Lett.* **43**, 5378–5384 (2016).
96. Guo, F., Liu, Q., Sun, S. & Yang, J. Three types of Indian Ocean Dipoles. *J. Clim.* **28**, 3073–3092 (2015).
97. Jiang, J. et al. Three types of positive Indian Ocean Dipoles and their relationships with the South Asian summer monsoon. *J. Clim.* **35**, 405–424 (2022).
98. Doi, T., Behera, S. K. & Yamagata, T. Predictability of the super IOD event in 2019 and its link with El Niño Modoki. *Geophys. Res. Lett.* **47**, e2019GL086713 (2020).
99. Zhang, Y. et al. Impact of the South China Sea summer monsoon on the Indian Ocean Dipole in CMIP5 models. *J. Clim.* **34**, 1963–1981 (2021).
100. Cai, W. & Cowan, T. Why is the amplitude of the Indian Ocean Dipole overly large in CMIP3 and CMIP5 climate models? *Geophys. Res. Lett.* **40**, 1200–1205 (2013).
101. Li, G., Xie, S.-P. & Du, Y. Climate model errors over the south Indian Ocean thermocline dome and their effect on the basin mode of interannual variability. *J. Clim.* **28**, 3093–3098 (2015).
102. Wang, G., Cai, W. & Santoso, A. Assessing the impact of model biases on the projected increase in frequency of extreme positive Indian Ocean Dipole events. *J. Clim.* **30**, 2757–2767 (2017).
103. McKenna, S., Santoso, A., Gupta, A. S., Taschetto, A. S. & Cai, W. Indian Ocean Dipole in CMIP5 and CMIP6: characteristics, biases, and links to ENSO. *Sci. Rep.* **10**, 11500 (2020).
104. Ng, B. & Cai, W. Present-day zonal wind influences projected Indian Ocean Dipole skewness. *Geophys. Res. Lett.* **43**, 11,392–311,399 (2016).
105. Qiu, Y., Cai, W., Li, L. & Guo, X. Argo profiles variability of barrier layer in the tropical Indian Ocean and its relationship with the Indian Ocean Dipole. *Geophys. Res. Lett.* **39**, https://doi.org/10.1029/2012GL051441 (2012).

106. Cai, W., Sullivan, A. & Cowan, T. Interactions of ENSO, the IOD, and the SAM in CMIP3 models. *J. Clim.* **24**, 1688–1704 (2011).
107. Jourdain, N. C., Lengaigne, M., Vialard, J., Izumo, T. & Gupta, A. S. Further insights on the influence of the Indian Ocean Dipole on the following year's ENSO from observations and CMIP5 models. *J. Clim.* **29**, 637–658 (2016).
108. Liu, L. et al. Indian Ocean variability in the CMIP5 multi-model ensemble: the zonal dipole mode. *Clim. Dyn.* **43**, 1715–1730 (2014).
109. Santoso, A., England, M. H., Kajtar, J. B. & Cai, W. Indonesian throughflow variability and linkage to ENSO and IOD in an ensemble of CMIP5 models. *J. Clim.* **35**, 3161–3178 (2022).
110. Sperber, K. et al. The Asian summer monsoon: an intercomparison of CMIP5 vs. CMIP3 simulations of the late 20th century. *Clim. Dyn.* **41**, 2711–2744 (2013).
111. England, M. H. et al. Recent intensification of wind-driven circulation in the Pacific and the ongoing warming hiatus. *Nat. Clim. Change* **4**, 222–227 (2014).
112. Power, S. et al. Decadal climate variability in the tropical Pacific: characteristics, causes, predictability, and prospects. *Science* **374**, eaay9165 (2021).
113. Capotondi, A. & Qiu, B. Decadal variability of the Pacific shallow overturning circulation and the role of local wind forcing. *J. Clim.* **36**, 1001–1015 (2023).
114. Allen, M. R. & Ingram, W. J. Constraints on future changes in climate and the hydrologic cycle. *Nature* **419**, 224–232 (2002).
115. Held, I. M. & Soden, B. J. Robust responses of the hydrological cycle to global warming. *J. Clim.* **19**, 5686–5699 (2006).
116. Vecchi, G. A. et al. Weakening of tropical Pacific atmospheric circulation due to anthropogenic forcing. *Nature* **441**, 73–76 (2006).
117. Knutson, T. R., Manabe, S. & Gu, D. Simulated ENSO in a global coupled ocean–atmosphere model: multidecadal amplitude modulation and CO_2 sensitivity. *J. Clim.* **10**, 138–161 (1997).
118. Johnson, N. C. & Xie, S.-P. Changes in the sea surface temperature threshold for tropical convection. *Nat. Geosci.* **3**, 842–845 (2010).
119. Zheng, X.-T., Xie, S.-P., Vecchi, G. A., Liu, Q. & Hafner, J. Indian Ocean Dipole response to global warming: analysis of ocean–atmospheric feedbacks in a coupled model. *J. Clim.* **23**, 1240–1253 (2010).
120. Cai, W. et al. Increased variability of eastern Pacific El Niño under greenhouse warming. *Nature* **564**, 201–206 (2018).
121. Zheng, X.-T., Lu, J. & Hui, C. Response of seasonal phase locking of Indian Ocean Dipole to global warming. *Clim. Dyn.* **57**, 2737–2751 (2021).
122. Endris, H. S. et al. Future changes in rainfall associated with ENSO, IOD and changes in the mean state over Eastern Africa. *Clim. Dyn.* **52**, 2029–2053 (2019).
123. Zhao, X. & Allen, R. J. Strengthening of the Walker circulation in recent decades and the role of natural sea surface temperature variability. *Environ. Res. Commun.* **1**, 021003 (2019).
124. Cai, W. et al. Changing El Niño–Southern Oscillation in a warming climate. *Nat. Rev. Earth Environ.* **2**, 628–644 (2021).
125. Cai, W. et al. Increased ENSO sea surface temperature variability under four IPCC emission scenarios. *Nat. Clim. Change* **12**, 228–231 (2022).
126. Marathe, S., Terray, P. & Karumuri, A. Tropical Indian Ocean and ENSO relationships in a changed climate. *Clim. Dyn.* **56**, 3255–3276 (2021).
127. Annamalai, H., Hamilton, K. & Sperber, K. R. The South Asian summer monsoon and its relationship with ENSO in the IPCC AR4 simulations. *J. Clim.* **20**, 1071–1092 (2007).
128. Li, X., Ting, M., Li, C. & Henderson, N. Mechanisms of Asian summer monsoon changes in response to anthropogenic forcing in CMIP5 models. *J. Clim.* **28**, 4107–4125 (2015).
129. Hui, C. & Zheng, X.-T. Uncertainty in Indian Ocean Dipole response to global warming: the role of internal variability. *Clim. Dyn.* **51**, 3597–3611 (2018).
130. Ng, B., Cai, W., Cowan, T. & Bi, D. Influence of internal climate variability on Indian Ocean Dipole properties. *Sci. Rep.* **8**, 13500 (2018).
131. Cai, W. et al. Anthropogenic impacts on twentieth-century ENSO variability changes. *Nat. Rev. Earth Environ.* **4**, 407–418 (2023).
132. Meehl, G. A. et al. The WCRP CMIP3 multimodel dataset: a new era in climate change research. *Bull. Am. Meteorol. Soc.* **88**, 1383–1394 (2007).
133. Taylor, K. E., Stouffer, R. J. & Meehl, G. A. An overview of CMIP5 and the experiment design. *Bull. Am. Meteorol. Soc.* **93**, 485–498 (2012).
134. Li, G., Xie, S.-P. & Du, Y. A robust but spurious pattern of climate change in model projections over the tropical Indian Ocean. *J. Clim.* **29**, 5589–5608 (2016).
135. Abram, N. J. et al. Palaeoclimate perspectives on the Indian Ocean Dipole. *Quat. Sci. Rev.* **237**, 106302 (2020).
136. IPCC, 2019: Summary for Policymakers. In *IPCC Special Report on the Ocean and Cryosphere in a Changing Climate* (eds Pörtner, H.-O. et al.) (IPCC, 2019).
137. Arias, P. et al. Technical Summary. In *Climate Change 2021: The Physical Science Basis. Contribution of Working Group I to the Sixth Assessment Report of the Intergovernmental Panel on Climate Change* (eds Masson-Delmotte, V. et al.) (Cambridge Univ. Press, 2021).
138. Abram, N. J., Gagan, M. K., Cole, J. E., Hantoro, W. S. & Mudelsee, M. Recent intensification of tropical climate variability in the Indian Ocean. *Nat. Geosci.* **1**, 849–853 (2008).
139. Abram, N. J., Gagan, M. K., McCulloch, M. T., Chappell, J. & Hantoro, W. S. Coral reef death during the 1997 Indian Ocean Dipole linked to Indonesian wildfires. *Science* **301**, 952–955 (2003).
140. Oppo, D. W., Rosenthal, Y. & Linsley, B. K. 2,000-year-long temperature and hydrology reconstructions from the Indo-Pacific warm pool. *Nature* **460**, 1113–1116 (2009).
141. Mohtadi, M. et al. North Atlantic forcing of tropical Indian Ocean climate. *Nature* **509**, 76–80 (2014).
142. DiNezio, P. N. et al. Glacial changes in tropical climate amplified by the Indian Ocean. *Sci. Adv.* **4**, eaat9658 (2018).
143. Thirumalai, K., DiNezio, P. N., Tierney, J. E., Puy, M. & Mohtadi, M. An El Niño mode in the glacial Indian ocean? *Paleoceanogr. Paleoclimatol.* **34**, 1316–1327 (2019).
144. Tierney, J. E. et al. The influence of Indian Ocean atmospheric circulation on Warm Pool hydroclimate during the Holocene epoch. *J. Geophys. Res. Atmos.* **117**, https://doi.org/10.1029/2012JD018060 (2012).
145. Tierney, J. E., Smerdon, J. E., Anchukaitis, K. J. & Seager, R. Multidecadal variability in East African hydroclimate controlled by the Indian Ocean. *Nature* **493**, 389–392 (2013).
146. Rustic, G. T., Koutavas, A., Marchitto, T. M. & Linsley, B. K. Dynamical excitation of the tropical Pacific Ocean and ENSO variability by Little Ice Age cooling. *Science* **350**, 1537–1541 (2015).
147. Cobb, K. M. et al. Highly variable El Niño–Southern Oscillation throughout the Holocene. *Science* **339**, 67–70 (2013).
148. Grothe, P. R. et al. Enhanced El Niño–Southern Oscillation variability in recent decades. *Geophys. Res. Lett.* **47**, e2019GL083906 (2020).
149. Brierley, C. M. et al. Large-scale features and evaluation of the PMIP4–CMIP6 *midHolocene* simulations. *Clim. Past.* **16**, 1847–1872 (2020).
150. Ying, J. et al. Emergence of climate change in the tropical Pacific. *Nat. Clim. Change* **12**, 356–364 (2022).
151. Geng, T. et al. Emergence of changing central-Pacific and eastern-Pacific El Niño–Southern Oscillation in a warming climate. *Nat. Commun.* **13**, 6616 (2022).
152. Wang, G., Cai, W. & Santoso, A. Variability of the Indian Ocean Dipole post-2100 reverses to a reduction despite persistent global warming. *Nat. Commun.* **15**, 5023 https://doi.org/10.1038/s41467-024-49401-y (2024).
153. Jochum, M. & Murtugudde, R. Temperature advection by tropical instability waves. *J. Phys. Oceanogr.* **36**, 592–605 (2006).
154. Moum, J. et al. Sea surface cooling at the Equator by subsurface mixing in tropical instability waves. *Nat. Geosci.* **2**, 761–765 (2009).
155. Holmes, R. M., McGregor, S., Santoso, A. & England, M. H. Contribution of tropical instability waves to ENSO irregularity. *Clim. Dyn.* **52**, 1837–1855 (2019).
156. Warner, S. J. & Moum, J. N. Feedback of mixing to ENSO phase change. *Geophys. Res. Lett.* **46**, 13920–13927 (2019).
157. Xue, A. et al. Delineating the seasonally modulated nonlinear feedback onto ENSO from tropical instability waves. *Geophys. Res. Lett.* **47**, e2019GL085863 (2020).
158. Cai, W. et al. Southern Ocean warming and its climatic impacts. *Sci. Bull.* **68**, 946–960 (2023).
159. Wang, G. et al. Future Southern Ocean warming linked to projected ENSO variability. *Nat. Clim. Change* **12**, 649–654 (2022).
160. Cai, W. et al. Antarctic shelf ocean warming and sea ice melt affected by projected El Niño changes. *Nat. Clim. Change* **13**, 235–239 (2023).
161. Planton, Y. Y. et al. Evaluating climate models with the CLIVAR 2020 ENSO metrics package. *Bull. Am. Meteorol. Soc.* **102**, E193–E217 (2021).
162. Liu, Y., Cai, W., Lin, X., Li, Z. & Zhang, Y. Nonlinear El Niño impacts on the global economy under climate change. *Nat. Commun.* **14**, 5887 (2023).
163. Cai, W. et al. Nonlinear country-heterogenous impact of the Indian Ocean Dipole on global economies. *Nat. Commun.* **15**, 5009 (2024).
164. Huang, B. et al. NOAA Extended Reconstructed Sea Surface Temperature (ERSST) Version 5 10.7289/V5T72FNM (NOAA National Centers for Environmental Information, 2017).

Acknowledgements

This work is funded by the Chinese Academy of Sciences (XDB40030000). G.W. and B.N. are supported by the Australian government under the National Environmental Science Program. N.A. is funded by the Australian Research Council (CE170100023 and SR200100008). K.Y. is funded by the National Natural Science Foundation of China (42105032). T.G. is supported by the National Natural Science Foundation of China project (42206209, 42276006) and the China National Postdoctoral Program for Innovative Talents (BX20220279). Y.D. is funded by the National Natural Science Foundation of China (42090042, 42149910 and 42049910) and the Chinese Academy of Sciences (133244KYSB20190031, 183311KYSB20200015). J.L. is supported by the National Natural Science Foundation of China (42288101). T.L. is supported by the National Natural Science Foundation of China (42088101). T.I. is funded by the Institut de Recherche pour le Développement (IRD). S.S. is funded by the National Natural Science Foundation of China (41976021). T.T. is funded by the JSPS KAKENHI (JP22K18727). X.Z. is funded by the National Natural Science Foundation of China (41975092). S.H. is funded by the National Natural Science Foundation of China (42022040).

Author contributions

G.W., W.C. and A.S. conceived the Review and coordinated the manuscript preparation, interpretation, discussion and writing. B.N., K.Y. and A.S. led the sections on the observed and simulated IOD processes. N.A. led the section on palaeoclimate data and created Fig. 6 with input from G.W. G.W. and T.G. conducted analysis and created Fig. 7. W.C. and G.W. led the remaining sections, and G.W. conducted analysis and generated other figures. All authors contributed to the manuscript preparation, interpretation, discussion and writing.

Competing interests

The authors declare no competing interests.

Additional information

Supplementary information The online version contains supplementary material available at https://doi.org/10.1038/s43017-024-00573-7.

Peer review information *Nature Reviews Earth & Environment* thanks Shanshan Liu, and the other, anonymous, reviewer(s) for their contribution to the peer review of this work.

[1]CSIRO Environment, Hobart, Tasmania, Australia. [2]Frontier Science Center for Deep Ocean Multispheres and Earth System (FDOMES) and Physical Oceanography Laboratory, Ocean University of China, Qingdao, China. [3]Laoshan Laboratory, Qingdao, China. [4]State Key Laboratory of Loess and Quaternary Geology, Institute of Earth Environment, Chinese Academy of Sciences, Xi'an, China. [5]State Key Laboratory of Marine Environmental Science & College of Ocean and Earth Sciences, Xiamen University, Xiamen, China. [6]Australian Research Council (ARC) Centre of Excellence for Climate Extremes and Climate Change Research Centre, University of New South Wales, Sydney, New South Wales, Australia. [7]International CLIVAR Project Office, Ocean University of China, Qingdao, China. [8]Research School of Earth Sciences, Australian National University, Canberra, Australian Capital Territory, Australia. [9]ARC Centre of Excellence for Climate Extremes, Australian National University, Canberra, Australian Capital Territory, Australia. [10]ARC Australian Centre for Excellence in Antarctic Science, Australian National University, Canberra, Australian Capital Territory, Australia. [11]State Key Laboratory of Numerical Modeling for Atmospheric Sciences and Geophysical Fluid Dynamics, Institute of Atmospheric Physics, Chinese Academy of Sciences, Beijing, China. [12]Application Laboratory (APL)/Research Institute for Value-Added-Information Generation (VAiG)/Japan Agency for Marine-Earth Science and Technology (JAMSTEC), Yokohama, Japan. [13]State Key Laboratory of Tropical Oceanography, South China Sea Institute of Oceanology, Chinese Academy of Sciences, Guangzhou, China. [14]University of Chinese Academy of Sciences, Beijing, China. [15]Institut de Recherche pour le Développement (IRD), UMR 241 SECOPOL IRD/UPF/IFREMER/ILM, Université de la Polynésie Française (UPF), Tahiti, French Polynesia. [16]Physical Sciences and Engineering, King Abdullah University of Science and Technology (KAUST), Thuwal, Saudi Arabia. [17]Centre for Earth, Ocean and Atmospheric Sciences, University of Hyderabad, Gachibowli, India. [18]Frontiers Science Center for Deep Ocean Multi-spheres and Earth System (DOMES)/Key Laboratory of Physical Oceanography/Academy of Future Ocean, Ocean University of China, Qingdao, China. [19]Department of Atmospheric Sciences, School of Ocean and Earth Science and Technology, University of Hawai'i at Mānoa, Honolulu, HI, USA. [20]Key Laboratory of Meteorological Disaster, Ministry of Education/Joint International Research Laboratory of Climate and Environmental Change/Collaborative Innovation Center on Forecast and Evaluation of Meteorological Disasters, Nanjing University of Information Science and Technology, Nanjing, China. [21]First Institute of Oceanography, Ministry of Natural Resources, Qingdao, China. [22]Qingdao Marine Science and Technology Center, Qingdao, China. [23]Shandong Key Laboratory of Marine Science and Numerical Modeling, Qingdao, China. [24]Department of Earth and Planetary Science, The University of Tokyo, Tokyo, Japan. [25]Key Laboratory of Ocean Observation and Forecasting, Key Laboratory of Ocean Circulation and Waves, Institute of Oceanology, Chinese Academy of Sciences, Qingdao, China. [26]Institute of Atmospheric Physics, Chinese Academy of Sciences, Beijing, China.